UNIVERSIDADE FEDERAL DE SANTA CATARINA
CAMPUS JOINVILLE
PROGRAMA DE PÓS-GRADUAÇÃO EM ENGENHARIA DE SISTEMAS ELETRÔNICOS

MATHEUS GAMA COSTA

# MULTIPHASE FLOW MEASUREMENTS BY VENTURI TUBE AND ULTRASONIC METERS

JOINVILLE
2020

Matheus Gama Costa

# MULTIPHASE FLOW MEASUREMENTS BY VENTURI TUBE AND ULTRASONIC METERS

Dissertação Submetida ao Programa de Pós-Graduação em Engenharia de Sistemas Eletrônicos da Universidade Federal de Santa Catarina para a obtenção do título de Mestre em Engenharia de Sistemas Eletrônicos.
Orientador: Prof. Kleber Vieira de Paiva, Dr.
Coorientador: Prof. Anderson W. Spengler, Dr.

Joinville
2020

Ficha de identificação da obra elaborada pelo autor,
através do Programa de Geração Automática da Biblioteca Universitária da UFSC.

Costa, Matheus Gama
Multiphase flow measurements by Venturi tube and Ultrasonic meters / Matheus Gama Costa ; orientador, Kleber Vieira de Paiva, coorientador, Anderson W. Spengler, 2020.
96 p.

Dissertação (mestrado) - Universidade Federal de Santa Catarina, Campus Joinville, Programa de Pós-Graduação em Engenharia de Sistemas Eletrônicos, Joinville, 2020.

Inclui referências.

1. Engenharia de Sistemas Eletrônicos. 2. Multiphase flows. 3. Flow pattern identification. 4. Flow rate measurements. 5. Venturi tube. I. Paiva, Kleber Vieira de . II. Spengler, Anderson W. . III. Universidade Federal de Santa Catarina. Programa de Pós-Graduação em Engenharia de Sistemas Eletrônicos. IV. Título.

Matheus Gama Costa

**Multiphase Flow Measurements by Venturi Tube and Ultrasonic Meters**

O presente trabalho em nível de mestrado foi avaliado e aprovado por banca examinadora composta pelos seguintes membros:

Prof. Jorge Luiz Goes Oliveira, Ph.D.
Universidade Federal de Santa Catarina

Prof. Rodrigo Moreira Bacurau, Dr.
Universidade Estadual de Campinas

Certificamos que esta é a **versão original e final** do trabalho de conclusão que foi julgado adequado para obtenção do título de mestre em Engenharia de Sistemas Eletrônicos.

_____

Coordenação do Programa de Pós-Graduação

_____

Prof. Kleber Vieira de Paiva, Dr.
Orientador

Joinville, 2020.

## ACKNOWLEDGMENT

This work would not have been possible without the financial support of PETROBRAS S.A.

I am especially grateful to Dr. Kleber Vieira de Paiva, my research advisor, who guided me patiently, encouraged me enthusiastically and strongly contributed to the development of this research work. As my teacher and mentor, he taught me more than I could ever give him credit for here.

I would also like to thank the collaboration of Dr. Jorge Luiz Goes Oliveira and Dr. Anderson W. Spengler during the development of this work. The training on using equipment, software, and theoretical knowledge in fluid dynamics and electronics were valuable to my professional growth.

My gratitude is also extended to André Luiz Alcantara Ostrufka, Giovani Silveira de Magalhães Martins, Guilherme Turatto, Leonel Edward Beckedorff, Ramon Peruchi Pacheco da Silva, Thiago Martins, Thiago Prestes Costa and Vinicius B. Zilli for their valuable technical support in this project.

I am also grateful to all those with whom I have had the pleasure to work during this period. That is why I must also thank all the staff of the T2F research group.

Thanks also to my friends for being always with me, even at a distance.

And finally, nobody has been more important to me in the pursuit of this project than the members of my family. I would like to thank my parents Eni Nudes da Gama and Vanilson Matos Costa, my sister Yasmin da Gama Costa, whose love and guidance are with me in everything I seek.

## RESUMO

A identificação de perfis de escoamento e a determinação das vazões mássicas de escoamentos multifásicos que chegam às plataformas de extração de petróleo e de gás natural são de suma importância para as empresas extrativas desses insumos. Equipamentos comerciais de medição multifásica são caros, aplicados em faixas restritas de medição e frequentemente não resistem às intempéries da aplicação, *e.g.* excesso de vibrações ou ambiente corrosivos. Dessa maneira, objetiva-se o desenvolvimento de sistemas de medição de baixo custo, com faixas de medição mais largas e capazes de suportar as condições desafiadoras de produção. Medições precisas e contínuas de escoamentos do tipo óleo-gás-água são essenciais para maximizar o controle do processo produtivo, além de evitar paradas de produção com fins de medição. O presente trabalho tem como objetivos caracterizar padrões de escoamentos e aferir vazão mássica de líquido em escoamentos do tipo líquido-gás a partir de técnicas ultrassônicas e de tubo de Venturi. Essas técnicas envolvem medições ultrassônicas em transmissão e recepção, e também em pulso eco. As técnicas de medição foram testadas em uma bancada de testes multifásica, permitindo escoamentos simultâneos de água e ar. A banca de testes é instrumentada com diversos sensores como medidores de vazão Coriolis e eletromagnético, termopares, transdutores de pressão e um tomógrafo de capacitância elétrica. A aquisição de dados e o controle da bancada foram realizados através de software LabVIEW. Testes em colunas estáticas também foram executados a partir de elementos piezoeléctricos e de uma placa TDC1000-7200 da *Texas Instruments*. Esta última permite a aferição do tempo de trânsito das ondas ultrassônicas na coluna de fluido, determinando a posição da interface e a concentração. Erros relativos menores que 10% foram obtidos na determinação da posição da interface em colunas de água e de petróleo bruto, respectivamente. Os maiores erros observados na determinação da posição da interface do petróleo bruto decorrem de incertezas em relação à velocidade do som com petróleo bruto utilizado. Nos testes dinâmicos, três padrões de escoamento líquido-gás foram testados: borbulhado, pistonado e estratificado. A identificação desses padrões foi possível através da aplicação da transformada rápida de Fourier (FFT) em sinais dinâmicos de concentração obtidos pelo tomógrafo e de pressão diferencial ao longo do tubo de Venturi. Aferições de vazão de líquido em escoamentos ar-água foram realizados a partir de tubo de Venturi e de medidor ultrassônico. Erros da vazão de líquido inferiores a 20% foram observados utilizando-se Venturi e para frações de vazio menores que 0,35; erros inferiores a 35% foram observados utilizando-se medidor ultrassônico. Aferições de vazão a partir de medidor ultrassônico somente foram possíveis para frações de vazio inferior a 0,18 em escoamentos horizontais, e inferiores a 0,32 em escoamentos verticais.



**Palavras-chave:** Escoamentos multifásicos; medidor ultrassônico; tubo de Venturi; medição de vazões; identificação de padrões de escoamento.

# RESUMO EXPANDIDO

## Introdução

Escoamentos multifásicos são encontrados em diversas aplicações de engenharia, desde o setor alimentício até o setor petroquímico. Neste último, observa-se frequentemente a presença de inúmeras fases, água e vários componentes de óleos e gases, em todo o percurso da produção. A aferição precisa dos fluxos mássicos dos insumos comercializáveis, petróleo e gás natural, é exigida pelas agências reguladoras. Medições precisas apenas são realizadas após intenso processo de separação e em interrupções do processo produtivo o que leva a perdas financeiras significativas. Dessa forma, existe a necessidade de desenvolver tecnologias que permitam a aferição precisa dos insumos comercializáveis sem a separação de fases e nos estágios iniciais de produção, reduzindo custos do processo produtivo e contribuindo para otimizações do controle da produção, e.g. atuação no sistema de injeção na rocha reservatório. Equipamentos alternativos dotados de novas e já conhecidas tecnologias são encontrados, porém são de alto custo. A busca por medidores precisos é comum entre empresas do setor, além do uso de tecnologias viáveis e soluções práticas no auxílio das operações de medição. Desse modo, observando-se as dificuldades nas medições de vazões em plataformas de petróleo e de gás natural, e seus benefícios na operação e no controle da produção, torna-se imperativo o desenvolvimento de equipamentos que sejam robustos, baratos e precisos. Também, é importante a utilização de sensores não intrusivos, de fácil mobilidade e que resistam a condições insalubres de produção como excesso de vibrações e ambiente corrosivo.

## Objetivos

Os objetivos principais do presente trabalho são identificar padrões de escoamento em escoamentos multifásicos e aferir com precisão a vazão de líquidos em escoamentos com a presença de gases por meio da integração de sensores ultrassônicos e um tubo de Venturi.

## Metodologia

Foram utilizados medidores ultrassônicos da marca GE Panametrics em modo transmissão-recepção e em pulso eco a partir de uma placa TDC1000-7200 da *Texas Instruments* para aferir concentrações de liquido em colunas estáticas. Esses medidores foram associados a um tubo de Venturi para aferir a vazão de líquido em escoamentos líquido-gás em uma bancada multifásica. Os testes estáticos foram realizados em uma caixa de aço inoxidável de 125x125x125 $mm^3$ para avaliar a capacidade de elementos piezelétricos em aferir a posição de interfaces entre fluidos com o objetivo de inferir concentrações. Foram utilizados água e petróleo bruto para aferir a fração volumétrica de líquidos e ar para a fração volumétrica de gás. Os testes dinâmicos foram realizados na bancada de escoamentos multifásicos presente no laboratório *Thermal Fluid Flow Group* - T2F. Escoamentos de água e ar em padrões pistonado, borbulhado e estratificado foram testados nas direções horizontal e vertical. As vazões de cada fase são obtidas através de medidores Coriolis instalados anteriormente ao ponto de mistura. As demais condições termodinâmicas são obtidas através de inúmeros transdutores de pressão e termopares instalados ao longo da bancada. Um tomógrafo de capacitância elétrica *Tomoflow ECT* permite a avaliação da concentração e das vazões de misturas. Estimativas das vazões de líquido em escoamentos água-ar através de técnicas ultrassônicas foram comparadas às medições de vazão por meio de medidor Coriolis. A identificação dos padrões de escoamentos foi possível através da aplicação da transformada

rápida de Fourier (FFT) em sinais dinâmicos de concentração obtidos pelo tomógrafo e de pressão diferencial ao longo do tubo de Venturi.

**Resultados e Discussões**

Nos testes em colunas estáticas, os elementos piezelétricos apresentaram um comportamento estável e com boa precisão. Erros menores que 10% foram obtidos na determinação da posição da interface em colunas de água e de petróleo bruto. Os maiores erros observados na determinação da posição da interface do petróleo bruto decorrem de incertezas em relação à velocidade do som no petróleo bruto utilizado. Em virtude de limitações do sistema de medição composto por transceptores piezelétricos, a detecção da interface somente foi possível em colunas de fluido superiores a 18 mm.

Nos testes dinâmicos, foi utilizado um tubo de Venturi para estimar a vazão de líquido em um escoamento de ar e água. A presença do ar no escoamento de água amplia o diferencial de pressão entre a entrada e a garganta do Venturi. Ao assumir escoamento monofásico e propriedades da água, a vazão de líquido calculada é superestimada. O erro relativo aumenta com o aumento da fração de vazio. Para uma fração de vazio igual a 0,35, o erro relativo é aproximadamente 20% para escoamentos horizontais.

Medições de vazão de líquido em escoamentos de ar e água somente foram possíveis para frações de vazio inferior a 0,18 em escoamentos horizontais, e inferiores a 0,32 em escoamentos verticais. A distribuição regular de fases em escoamentos verticais favorece a propagação do pulso mecânico através do meio líquido. Erros relativos inferiores a 35% foram observados utilizando-se o medidor ultrassônico.

Nos testes dinâmicos, três padrões de escoamento líquido-gás foram testados: borbulhado, pistonado e estratificado. A identificação desses padrões foi possível através da aplicação da transformada rápida de Fourier (FFT) em sinais dinâmicos de concentração obtidos pelo tomógrafo e de pressão diferencial ao longo do tubo de Venturi. Alto conteúdo de energia é observado em maiores frequências (15 Hz) para escoamentos borbulhados, e em menores frequências (8 Hz) para o padrão estratificado, nas presentes condições experimentais com temperatura de 23 °C e pressão de gás e água iguais. Em padrões pistonados, alto conteúdo de energia foi observado em frequência intermediárias (10 Hz). A identificação dos padrões de escoamento é também possível através dos valores de desvio padrão da pressão diferencial no Venturi.

**Considerações Finais**

A aquisição de dados e o controle da bancada experimental foram realizados através de software LabVIEW. Códigos para permitir a obtenção e a extração de informações úteis dos sinais piezelétricos foram desenvolvidos. A identificação de concentração estática de liquido e gás foi realizada utilizando transmissores/receptores piezelétricos. Escoamentos de ar e água foram gerados para três padrões: borbulhado, pistonado e estratificado. A caracterização desses escoamentos foi realizada a partir de medições de pressão diferencial em tubo de Venturi, utilização de tomógrafo de capacitância elétrica, termopares, transdutores de pressão e dos medidores Coriolis posicionados antes da formação da mistura bifásica.

O tomógrafo de capacitância elétrica Tomoflow ECT foi calibrado para operar com água e ar. A resolução espacial do tomógrafo da ordem de 1mm foi suficiente para caracterizar imagens de padrões pistonado e estratificados. Dessa forma, valores precisos de concentração foram determinados para todos os padrões.

**Palavras-chave:** Escoamentos multifásicos; medidor ultrassônico; tubo de Venturi; medição de vazões; identificação de padrões de escoamento.

## ABSTRACT

Flow pattern identification and inline multiphase flow measurements are essential matters regarding design and production control of oil and gas rigs. Multiphase flow measuring equipment are expensive, often fragile and applied in tight measuring ranges. Therefore, the development of low cost measuring systems with wider measuring ranges and capable of withstanding the challenging production conditions is essential to oil and gas industry. Accurate and continuous oil-gas-water flow measurements are critical for maximizing process control and avoiding production stoppages for metering purposes. The present work aims at characterizing flow patterns and measuring liquid mass flow rate in liquid-gas flows using ultrasonic sensors and a Venturi tube. Ultrasonic waves is applied in transmission and reception mode, and in pulse echo approaches. Measurement techniques were tested on an experimental bench where water, oil and air multiphase flows are possible. The experimental rig is instrumented with various sensors such as Coriolis and electromagnetic flow meters, thermocouples and pressure transducers. Liquid and gas instantaneous flow images are possible due to electrical capacitance tomography (ECT) technique. Data acquisition were performed using LabVIEW software. Experiments in static columns were executed with piezoelectric sensors and a TDC1000-7200 board from Texas Instruments. The latter allows transit time measurement of ultrasonic waves in the fluid column, determining the interface position and concentration. The interface position of water and crude oil columns were determined with relative errors less than 10%. Higher errors for determining the crude oil interface occurred owing to uncertainties regarding the sound speed in the applied crude oil. Bubbly, slug and stratified flow patterns were tested at the multiphase setup. Flow pattern identification was possible through the application of the fast Fourier transform (FFT) on concentration signals obtained by ECT and on differential pressure signals along the Venturi tube. Liquid flow rate measurements were performed in air-water flows with the aid of a Venturi tube and an ultrasonic meter. Errors of liquid flow rate below 20% were observed with the Venturi meter for void fractions less than 0.35. Errors below 35% were noted with ultrasonic sensors. Liquid flow rate assessments by means of ultrasonic meters were only possible for void fractions less than 0.18 in horizontal direction, and less than 0.32 in vertical direction.



**Keywords:** Multiphase flows; ultrasonic sensors; Venturi tube; flow rate measurements; flow pattern identification.

## FIGURES LIST

## TABLE LIST

**TABLE OF CONTENTS**

# 1 INTRODUCTION

Multiphase flows are found in countless engineering applications from food to petrochemical sectors. In the latter, several gases, oil components and water coexist within pipelines and processing equipment. The design and production control of oil and gas rigs would improve if inline multiphase flow measurements could be performed with high precision and for a wide measuring range. With a better production control, and less time consumption in the measurement. Multiphase flow measuring equipment are expensive, often fragile and applied in tight measuring ranges. Therefore, the development of low cost inline measuring systems with wider measuring ranges and capable of withstanding the challenging production conditions is essential to oil and gas industry. Accurate and continuous oil-gas-water flow measurements are critical for maximizing process control and avoiding production stoppages for metering purposes. Furthermore, accurate measurements may allow control actions on valves, water injection in oil wells, among others (FOSS; KNUDSEN; GRIMSTAD, 2018).

Currently, separator tanks are commonly used to estimate the well production rates. During the measurement period the production must be stopped. After the separation of each phase, single-phase measurement techniques are employed to estimate the production rates within the defined measurement time interval (CORNELIUSSEN et al. 2005).

In-line mass flow rate measurements are desirable in the oil and gas industry in order to maximize production through real-time monitoring, excluding conventional separation systems (OLIVEIRA et al., 2009). Alternative equipment with new and well-known technologies are found but they are costly and applied in tight measuring ranges (LORENTZEN et al., 2010). Thus, research of low cost and accurate meters is common among companies in the sector. The use of viable technologies and practical solutions to support the measurement operations may also reduce foot-print area and costs of extraction operation. In addition to accuracy and robustness, low cost and non-intrusive characteristics are desirable. Data transmission and storage also needs to be addressed.

The present work aims at characterizing flow patterns and measuring liquid mass flow rate in liquid-gas flows using transmission-reception ultrasonic sensors and a Venturi tube. Ultrasonic time of flight (ToF) sensors will be applied in pulse echo approach. A custom-made electronic system was developed to read signals from piezoelectric sensors. Measurement techniques were tested on an experimental rig where water, oil and air

multiphase flows are possible. Bubbly, slug and stratified flow patterns were tested at the multiphase setup. Experiments in static columns were executed with piezoelectric sensors and a TDC1000-7200 board from Texas Instruments. Flow pattern identification was possible through the application of the fast Fourier transform (FFT) on concentration signals obtained by ECT and on differential pressure signals along the Venturi tube.

## 1.1 GOALS

### 1.1.1 Main Goals

The main objectives of the present work are to identify flow patterns and to determine the liquid mass flow rate in liquid-gas flows by means of non-commercial ultrasonic sensors integrated with a Venturi tube.

### 1.1.2 Specific Goals

The specific objectives are as follows:

- Determination of gas-liquid interface positions and concentrations by the use of piezoelectric sensors in static columns;
- Design of a custom-made electronic system to read signals from piezoelectric sensors;
- Determination of liquid flow rate in gas-liquid flows by means of a Venturi tube;
- Determination of liquid flow rate in gas-liquid flows by means of Ultrasonic sensors;
- Identification of limiting void fractions for ultrasonic measurements in horizontal and vertical directions;
- Flow pattern identification by means of pressure difference signals from a Venturi tube;
- Flow pattern identification by means of concentration signals from an Electrical Capacitance Tomography;
- Execution of static tests with water, crude oil and air as to identify concentrations of each one;
- Execution of dynamic tests in a multiphase flow rig.

# 2 THEORETICAL FRAMEWORK

## 2.1 MULTIPHASE FLOWS

Multiphase flows are defined as fluid flows where two or more phases are present simultaneously. The phases can be combinations of liquids, gases or solids. Analyses of multiphase flows are more complex than single-phase flow investigations due to the following features:

- Additional number of equations owing to the presence of more than one phase;
- Complex spatial distribution of phases;
- Presence of interfaces, particularly gas-liquid interfaces;
- The flow pattern effect on the domain characteristics: velocity, temperature, pressure and concentration distributions. Variation of local variables are often more intense than in single-phase flows;
- Occurrence of complex phenomena such as phase change, collisions, surface tension effects etc.

Thus, measurements of multiphase flow variables are complex due to the mass, momentum and energy transfer among the phases, Christopher (2005). Direct and precise determination of water, oil, and air mass flow rates without phase separation in the oil and gas industry is costly, uncommon and restricted to tight measuring ranges (LORENTZEN et al., 2010).

The total volumetric flow rate, $\dot{Q}$, of a multiphase flow consisting of three phases is defined in internal flow as:

$$\dot{Q} = A.\left(\alpha.v_g + \beta.v_w + \gamma.v_o\right) \quad (1)$$

where A is the duct cross-sectional area, α, β and γ are the phase concentrations, $v_g$, $v_w$ e $v_o$ are the mean bulk velocities of each phase. The subscripts *g*, *w* and *o* stand for gas, water and oil, respectively. Since α + β + γ = 1, the measurement of two phase concentrations are sufficient for measurement purposes (THORN; JOHANSEN; HJERTAKER, 2012). Equation 1 can be rewritten as:

$$\dot{Q} = A.\{\alpha.v_g + \beta.v_w + [1-(\alpha+\beta)].v_o\} \quad (2)$$

The total mass flow rate, $\dot{M}$, of a multiphase flow consisting of three phases is defined as:

$$\dot{M} = A.\{\alpha.v_g.\rho_g + \beta.v_w.\rho_w + [1-(\alpha+\beta)]v_o.\rho_o\} \quad (3)$$

where $\rho$ is the mass density.

Mass flow rates of multiphase flows can be determined indirectly. Independent methods are often used to obtain mass densities, volumetric fractions and average bulk velocities of each phase present in the flow. Figure 1 presents a schematics of mass flow rate determination in a multiphase flow.

Figure 1 - Schematics of mass flow rate determination in a multiphase flow.

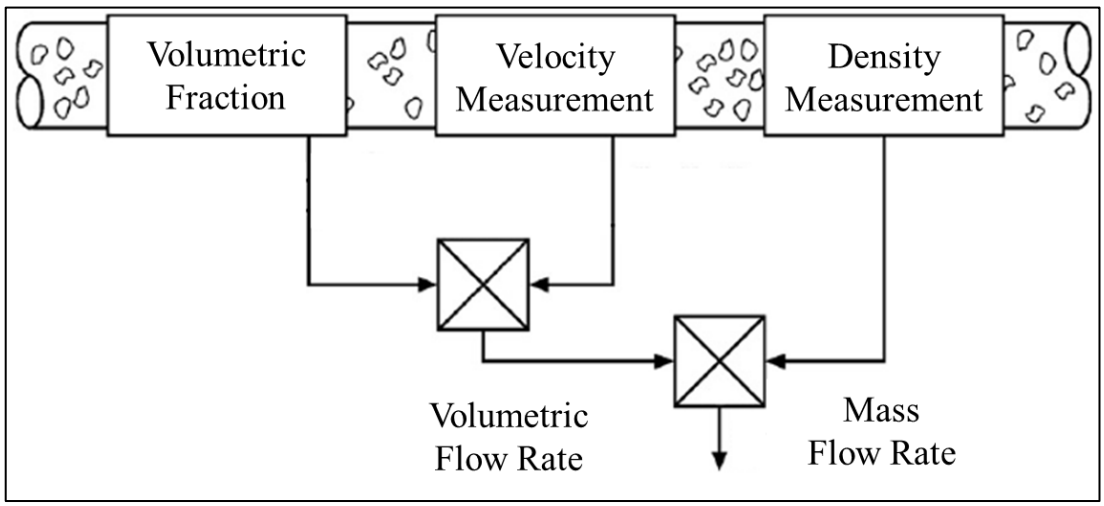


Source: Adapted, Thorn; Johansen; Hjertaker (2012).

### 2.1.1 Multiphase Flow Patterns

Flow patterns in the oil and gas industry are rather complex. Several gases, liquids and solids components are present in multiphase flows at this industry. Oil in wells consist of mixtures of heavy hydrocarbons, while gases consist of mixtures of light hydrocarbons, dioxide carbon among others. Solids as sand particles can be neglected in the present analysis. Depending on the thermodynamic conditions, oil composition and volumetric concentrations of each phase, different emulsion processes occur during the extraction along the pipelines

and processing equipment. These processes affect phase distribution and therefore the actual flow pattern.

With the aim of facilitating the present analysis, flow patterns will be classified as two-phase gas-liquid flows. Oil components and water will be treated as a single liquid phase, and the mixture of gases, as a single gas phase.

Two-phase gas-liquid flow regimes can be classified into three main categories: dispersed, separate and intermittent, or a combination of them, see Corneliussen et al. (2005). Their descriptions are given as follows:

- *Dispersed flow*: characterized by a uniform phase distribution along radial and axial directions;
- *Separate flow*: characterized by a non-continuous phase distribution along radial and streamwise directions;
- *Intermittent flow*: characterized by flow instabilities and non-continuous behavior along streamwise direction.

Flow patterns are often determined by visual inspection. In situations where visual information is not sufficient for pattern classification, analysis of volumetric fraction signals has been used to configuration recognition (CORNELIUSSEN, et al. 2005).

In order to predict the occurrence of a given flow pattern, flow pattern maps are applied. Several parameters can affect and determine an actual gas-liquid flow pattern: pipe dimensions (e.g. hydraulic diameter), pipe inclination, thermodynamic conditions (i.e. pressure and temperature), flow regime (i.e. laminar, transitional or turbulent), phase distributions (e.g. concentrations and velocities) and surface tension effects, see Christopher (2005). Examples of flow pattern maps for gas-liquid flows in pipes are presented in the next sections.

#### 2.1.1.1 Flow Patterns in Vertical Direction

Figure 2 presents an example of gas-liquid flow pattern map for flows in vertical direction, see Corneliussen et al. (2005). Depending on the superficial gas and liquid velocities, bubbly, finely dispersed bubbly, slug, churn and annular flow patterns can occur.

Figure 2 - Example of gas-liquid flow pattern map for flows in vertical direction.

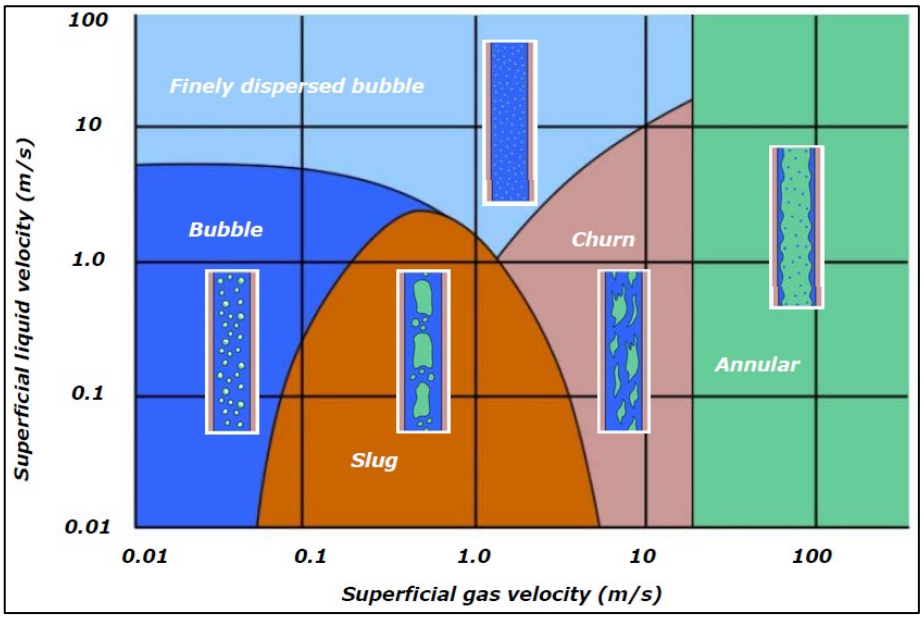


Source: Corneliussen et al. (2005).

Collier and Thome (1996) described gas-liquid flow patterns in vertical direction as follows:

- *Bubbly flow:* the gas or vapor phase is distributed as discrete bubbles in a continuous liquid phase. Bubbles may be small and spherical or large with a flattened tail;
- *Slug flow*: gas or vapor large bubbles occupy approximately the pipe diameter. The bubble upper part is spherical and separated from the duct wall by a thin liquid film. Two successive large bubbles are separated by slugs that may contain small bubbles in dispersed form;
- *Churn flow*: characterized by slug flow instability and intense break-up occurrence. A chaotic gas flow occurs in the pipe center, moving liquid towards the pipe walls. This pattern presents combined aspects of slug and annular flow patterns;
- *Annular flow*: characterized by gas flow through the pipe core and continuous liquid film surrounding the pipe wall. Large amplitude waves may occur on the liquid-gas interface. The continuous breakage of these waves form a source of droplet entrainment into the central gas core;
- *Mist flow*: characterized by gas flow with the liquid phase distributed as droplets in a continuous gaseous phase.

2.1.1.2 Flow Patterns in Horizontal Direction

Figure 3 presents an example of gas-liquid flow pattern map for flows in horizontal direction, see Corneliussen et al. (2005). The gravity acceleration perpendicular to flow direction affects flow pattern occurrence. Depending on the superficial gas and liquid velocities, bubbly, slug, plug, stratified, wave, mist and annular flow patterns can occur.

Figure 3 - Example of gas-liquid flow pattern map for flows in horizontal direction.

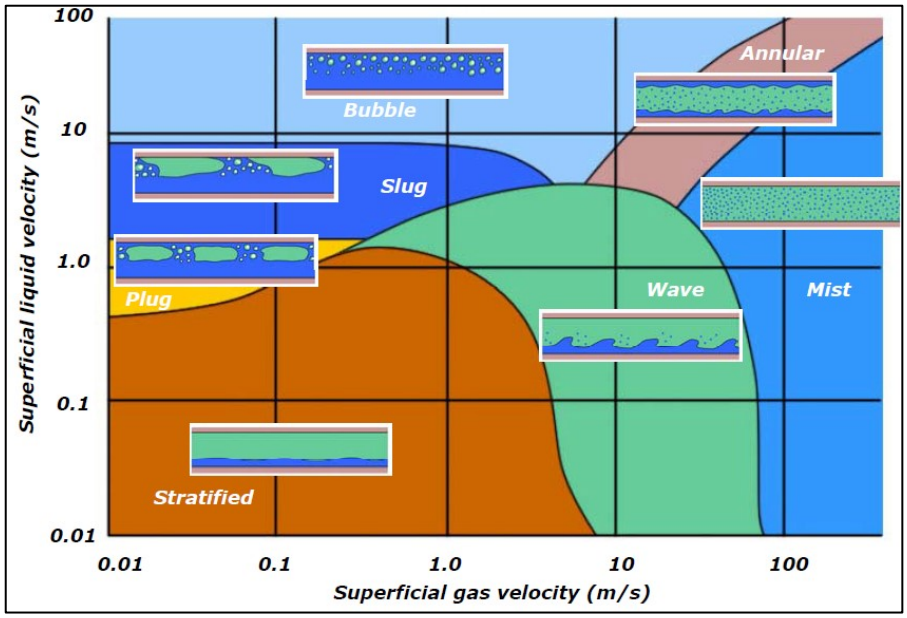


Source: Corneliussen, et al. (2005).

Collier and Thome (1996) described gas-liquid flow patterns in horizontal direction as follows:

- *Bubbly flow*: similar to that shown in vertical flow direction, except that the vapor or gas bubbles mainly occur at the top part of the pipe cross-section;
- *Plug flow*: similar to slug flow in vertical flow direction. Gas bubbles mainly occur at the top part of the pipe cross-section;
- *Stratified flow*: It occurs only at very low liquid and gas bulk velocities. Two phases flow separately with a relatively smooth interface;
- *Wavy flow*: a separate two-phase flow characterized by waves created by disturbances at the gas-liquid interface owing to increasing gas velocity;
- *Slug flow*: characterized by slugs propagated along the channel at high velocities. The liquid phase between two consecutive slugs fill the entire pipe cross-section often with

small spherical and dispersed bubbles. The large gas bubbles are formed from the destabilization of the liquid film. This pattern should not be confused with plug flow in horizontal ducts. In this case, large bubbles are formed from the coalescence of small ones;

- *Annular flow*: characterized by gas flow through the pipe core and continuous liquid film surrounding the pipe wall. Large amplitude waves may occur on the liquid-gas interface. The continuous breakage of these waves form a source of droplet entrainment into the central gas core. The liquid film may be thicker at the bottom part of the pipe cross-section;
- *Mist flow*: characterized by gas flow with the liquid phase distributed as droplets in a continuous gaseous phase.

## 2.2 VELOCITY MEASUREMENT WITH VENTURI METER

Bulk velocity or flow rate measurements by means of cross-section reduction in internal flows are a well-known technique for single-phase flows. Owing to the flow acceleration it is possible to relate the bulk velocity to the pressure difference across the measurement device. Bulk velocity and pressure difference are linked via the continuity, Bernoulli and energy equations, and by introducing a correction coefficient to account for dissipation effects. The correction coefficient or discharge coefficient, $C_d$, is defined as a function of Reynolds number based on the bulk velocity and the pipe diameter. Values of $C_d$ for Venturi meters can be as high as 0.99.

Employment of Venturi meters for single-phase flows is defined in ISO 5167. Fully developed flow is necessary for appropriate application of differential pressure meters. Several pipe diameters are required until the flow becomes stationary. The necessary length needed for fully developed flow is called hydrodynamic inlet region; see schematics in Figure 4. ISO 5167 recommends the installation of flow conditioners in the pipe entrance towards the meter in order to remove side effects (e.g. disturbances induced by valves, bends, expansions and contractions) as to reduce the hydrodynamic inlet length.

Figure 4 - Schematics of the hydrodynamic inlet region in a pipe.

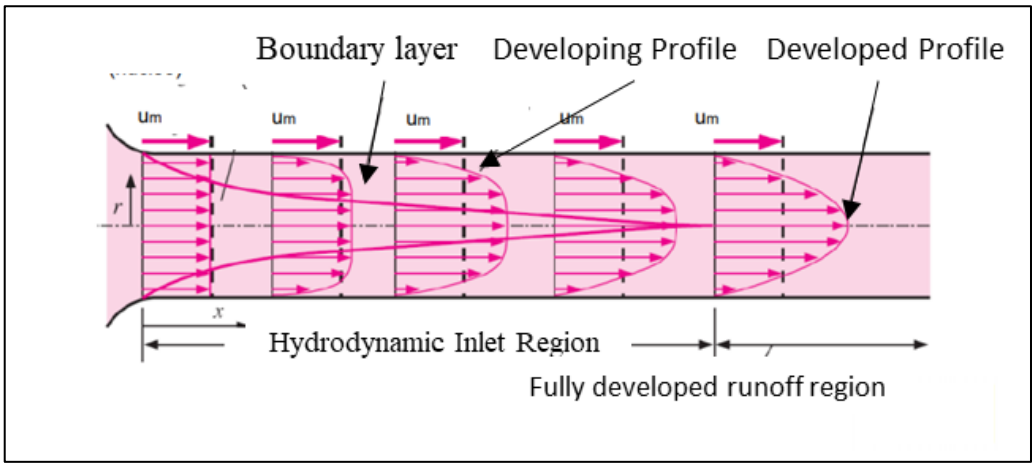


Source: Adapted, Çengel, et al. (2007).

The Venturi geometry consists of a short converging section followed by the throat and a long diverging section; see an illustration example in Figure 5. Pressure taps are located at the pipe entrance and at the throat. In the diverging section, the bulk flow velocity reduces while the static pressure increases. The diverging section is longer as to reduce the increasing pressure gradient in streamwise direction, avoiding boundary layer detachment.

Figure 5 – Illustration of a typical Venturi geometry.

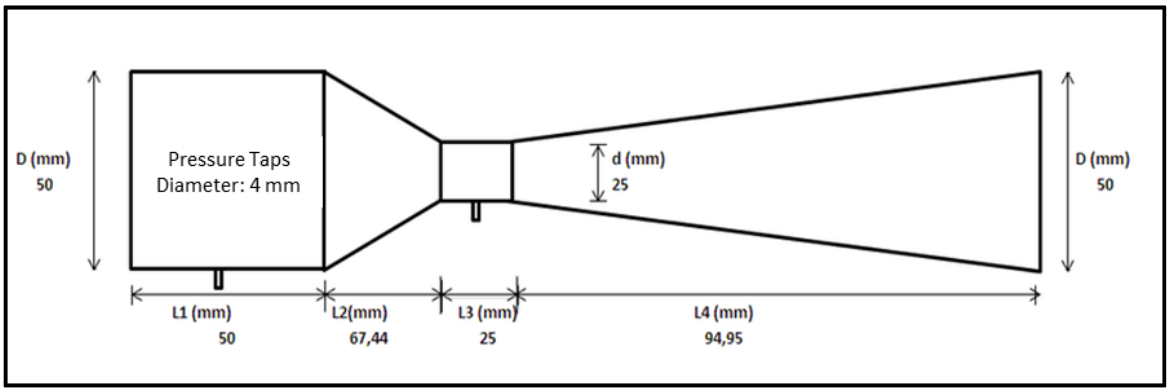


Source: Santos; Bettega (2015)

## 2.3 COMPUTED TOMOGRAPHY

Computed Tomography (CT) is related to the imaging reconstruction by sectioning, through the use of any kind of penetrating wave (SOUSA, 2017). Over the past few decades, CT technologies became popular in medical applications, although it is applied in areas such as geophysics, oceanography, plasma physics, materials science, astrophysics etc.

Several types of techniques are applied on computed tomography; see few examples in Table 1, Beck & Williams (1996).

Table 1 – Examples of techniques employed in computed tomography.

| **Types of Tomography** | **Typical Spatial Resolution** (percentage of the section diameter) | **Source of Data** | **Features** |
|---|---|---|---|
| Electromagnetic radiation | 1% | X-rays and γ-rays<br>Positron Emission<br>Magnetic Resonance | Slow<br>Contaminating Radiation<br>'Marked' particles<br>Quick<br>Expensive for large volumes |
| Acoustics | 3% | Ultrasound | Limited propagation speed<br>Complex use |
| Electrical | 10% | Capacitance<br>Resistivity<br>Impedance | Quick<br>Low cost<br>Useful for small and large volumes |

Source: Beck; Williams (1996).

In the oil and gas industry, tomography technologies can also be applied to multiphase flow measurements. Among the CT technologies specified above, Electrical Capacitance Tomography (ECT) is appropriate owing to the fine time resolution and since oil and gas properties are adequate for this technique (BECK; WILLIAMS, 1996). Often the ECT time resolution is sufficient to describe local flow rates and the spatial distribution of phases.

### 2.3.1 Electrical Capacitance Tomography

The variation of electrical permittivity in a region of study allows the use of electrical techniques for tomographic measurement (SOARES, 2009). In ECT tomography, multiple electrodes are mounted around the region of analysis; see an illustration in Figure 6. Differently from resistive impedance, capacitive sensors can work at high frequencies. In fluid flow applications, the capacitive electrodes are not in contact with the working fluid. The surface of conductive electrodes, the distance between them and the dielectric characteristics of each fluid inside the measuring volume affect the measurements of a capacitor (WARREN; WILCOX, 2006).

For multiphase flows in the oil and gas industry, the relative permittivity or dielectric constant $\varepsilon_r$ of flow components ranges from 1 for air to 80 $Fm^{-1}$ for water (WARNER;

WILCOX, 2006). The relative permittivity of remaining gases and oil components are within this range. The absolute permittivity ε can be obtained with the vacuum permittivity ($\varepsilon_0 \approx 8.854218781 \times 10^{-12}\ Fm^{-1}$):

$$\varepsilon = \varepsilon_r * \varepsilon_0 \tag{5}$$

Figure 6 – Illustration of an arrangement of sensors for tomographic applications. 12-electrode capacitive sensors are applied on this arrangement.

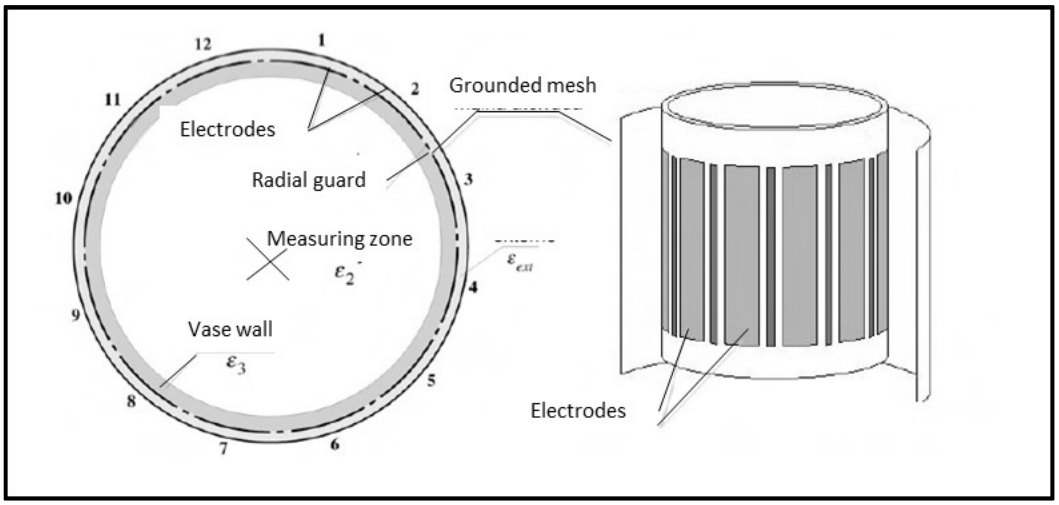


Source: Soares (2009).

Figure 7 presents a schematic of an ECT tomographic system. Sensors in the measurement volume (a) are connected to capacitive measurement appliances (c). Data is transferred to a computer (d) via transduction electronics (b). Dedicated algorithms are applied to allow imaging reconstruction (CAVALCANTI, et al. 2009).

Figure 7 - Schematic of an ECT tomographic system - a) sensors; b) transduction electronics; c) capacitive measurement appliances d) computer for data processing and imaging reconstruction.

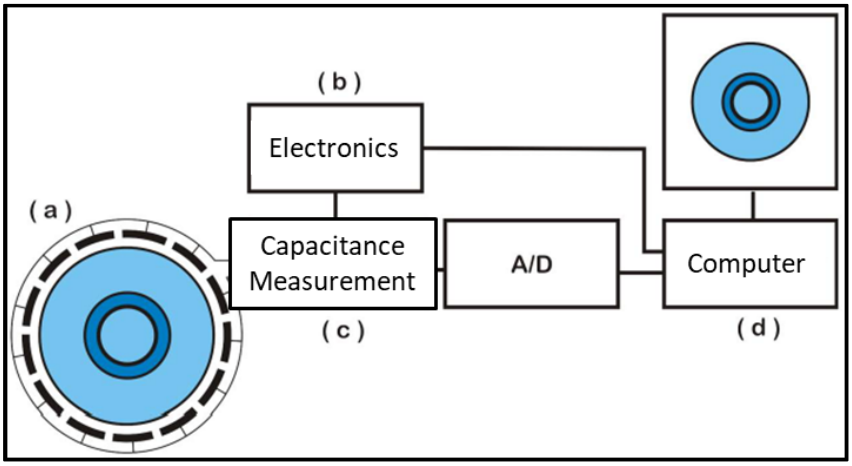


Source: Cavalcanti et al. (2009).

Algorithms correlate permittivity data measurements to fluid distributions within the measurement volume, reconstructing flow images. The oldest and simplest projection reconstruction method is the linear back projection (LBP), see Hayes et al. (1995) and Green (1990), for example. Besides LBP, other techniques can be employed such as multilayer perceptron neural networks (CAVALVANTI et al., 2009).

## 2.4 ULTRASONIC WAVES

Ultrasonic waves are mechanical waves that propagate at frequencies greater than 20 kHz. They are generally generated from disturbances in a material and they can propagate longitudinally or transversely through solids. Through fluids sound often travels as longitudinal waves, vibrating in the same direction as that of propagation (DACIUK, 2008).

Ultrasonic waves can be generated by piezoelectric effect, converting an electrical pulse into mechanical vibration using piezoelectric crystal transducers. The same piezoelectric material can also act as an ultrasonic receiver by converting mechanical energy into an electrical signal. When the wave crosses the interface between two materials with different characteristics, energy reflection and transmission may occur as well as change on propagation direction (DACIUK, 2008).

At liquid-gas interfaces an ultrasonic wave is reflected almost entirely. This remark allows gas bubble detection in two-phase flows. Ultrasonic techniques can be classified into

three main types in flow analysis: Doppler, transmission-reception and pulse-echo. Their combination can also be used, resulting in a hybrid method (DACIUK, 2008).

### 2.4.1 Doppler

The Doppler effect is the change in frequency of a wave with regard to an observer, moving relatively to the wave source. The difference between the transmitted and received wave frequency is directly related to the bulk flow velocity. Through a known geometry, it is possible to obtain the mean flow velocity (MURAKAWA et al. 2005). Figure 8 exemplifies the Doppler effect, where O is the observer and A, the emitting source.

Figure 8 – Illustration of Doppler effect with a stationary observer.

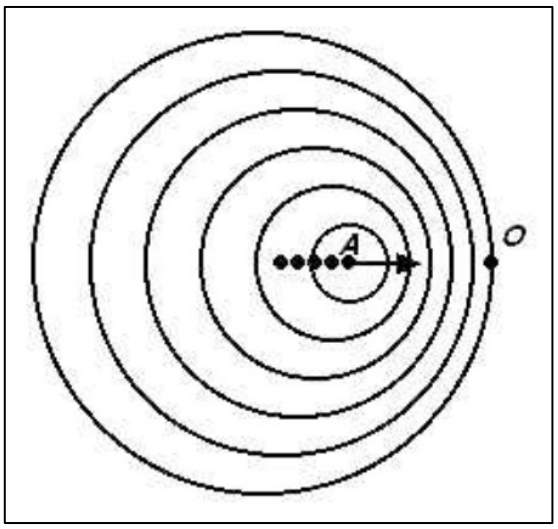


Source: Adapted, Halliday e Resnick (2012).

The relationship between observed frequency $f'$ and emitted frequency $f$ is given by (HALLIDAY e RESNICK, 2012):

$$f' = f.\frac{v \pm v_D}{v \pm v_F} \tag{7}$$

where $v$ is the propagation velocity of waves in the medium , $v_D$, the receiver velocity relative to the medium and $v_F$, the source velocity relative to the medium. Figure 9 presents an example of the employment of ultrasound Doppler technique for flows with dispersed bubbles in pipes.

Figure 9 - An example of the employment of ultrasound Doppler technique for flows with dispersed bubbles in pipes.

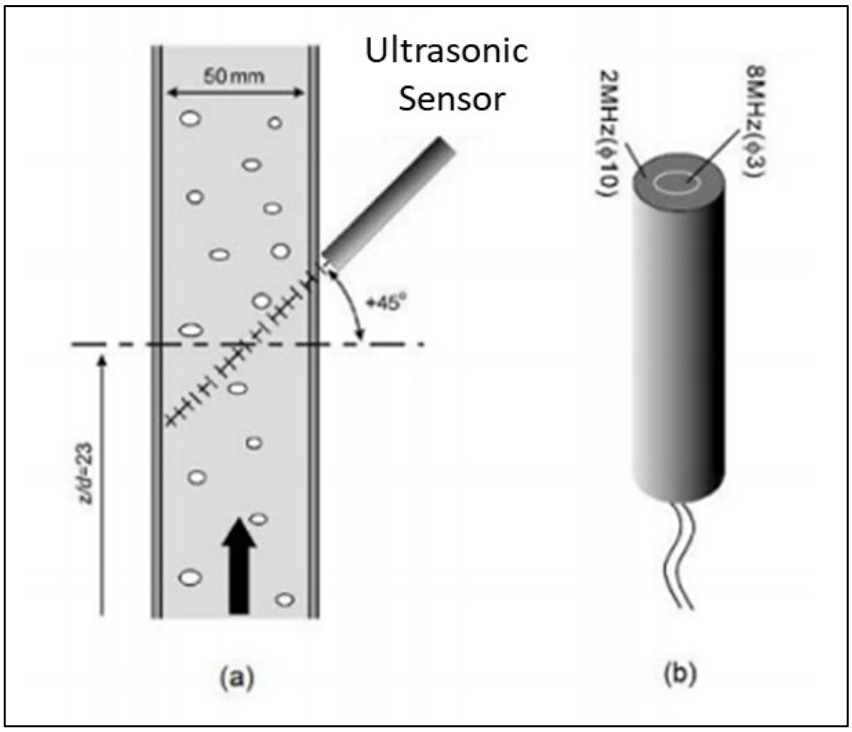


Source: Murakawa et al. (2005).

Bulk flow velocity measurements is possible in flows with dispersed bubbles or solid particles (MURAKAWA et al, 2005). Bulk flow velocity $V$ can be calculated as:

$$V = v.\frac{(f_r - f_t)}{(2.f_t.\cos\theta)} \tag{8}$$

where $f_r$ is the frequency of the scattered ultrasound beam, $f_t$, the frequency of the transmitted ultrasound beam , $v$, the sound velocity in the medium and $\theta$, the intercept angle between the ultrasonic beam and the main flow direction.

Doppler meters are suitable for measuring liquid flow rates with dispersed phase as suspended solids (LIPTAK, 2003). This method is non-intrusive and the power consumption is minor. Several disadvantages can be related as the dependence on fluid properties and on particle density. A non-uniform particle distribution in the pipe cross-section can result in an incorrect mean flow velocity.

### 2.4.2 Transmission-Reception

Transmission-reception ultrasound technique comprises the propagation of ultrasonic waves generated from an emitter and acquired by one or more opposite receivers. For flow velocity measurements, emitter and receiver transducers must be inclined regarding the main flow direction. Figure 10 presents a typical configuration of flow velocity measurement, with sensors A and B positioned at an angle δ formed between a fictitious line along the emitter-receiver centers and the pipe axis.

Figure 10 - Illustration of transmission-reception ultrasound technique for flow velocity measurement.

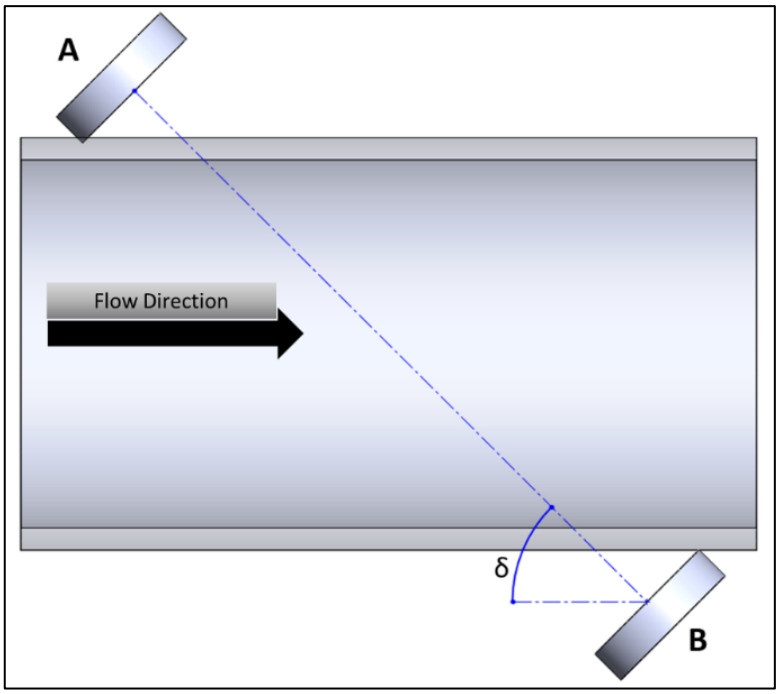


Source: Author (2020).

Brassier, Hosten, and Vulovic (2001) used an arrangement similar to the one shown in Figure 10 to perform measurements in multiphase flows. Bulk flow velocities in pipes were obtained with relative errors less than 1.5% for volumetric flows in the range 250-1000 m³/h. The mean flow velocity $V$ is given by:

$$V = [\Delta t/(t_1.t_2)].[L/(2\cos\delta)] \quad (9)$$

where $L$ is the distance between the emitter and receiver centers, $D$, the pipe diameter, $\Delta t$, the transit time difference, $t_1$ and $t_2$ are the absolute transit times of sensors 1 and 2, in that order.

With the configuration shown above, it is possible to detect interfaces in liquid-gas flows as well as to obtain the mean bulk flow velocity and the average void fraction. They can be obtained through correlations that relate the transit time change to the wave amplitude. Vatanakul et al. (2004) related the transit time standard deviation to the ultrasound signal amplitude as to obtain the void fraction in three-phase flows.

### 2.4.3 Pulse-Echo

In ultrasonic pulse-echo technique, a wave is emitted from a piezoelectric transducer, and its echo (a reflection from another surface) is detected by the same transducer at later time, after the wave propagate inside the liquid and return; see Janiga *et al*. (2019). In multiphase flows, this technique has been applied to determine interface positions of different phases. Through mechanical energy variation induced by wave reflection on dispersed bubbles or particles, it is possible to characterize mixture parameters such as volumetric phase fractions (DACIUK, 2008).

The transit time of ultrasonic signals relies on the liquid column and on the pipe wall thickness; see Faccine (2008) for example. The wall influence needs to be extracted from the total wave travelling time. For proper measurements, it is necessary *a priori* knowledge of sound velocities in both the pipe wall and in the liquid column. Figure 11 shows an illustration of typical pulse-echo arrangements in pipes.

Figure 11 - Illustration of typical pulse-echo arrangements in pipes.

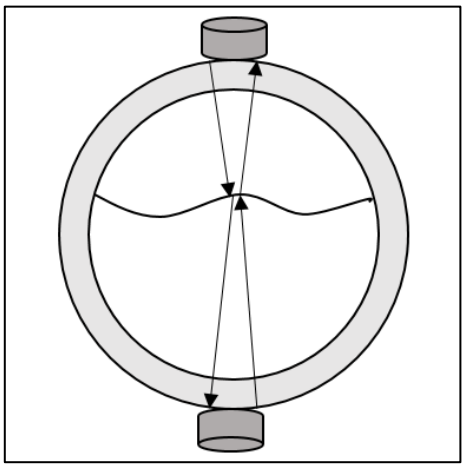

Source: Author (2020).

In ultrasonic pulse-echo technique, increasing attenuation of mechanical energy can be correlated to increasing volumetric fraction of the dispersed phase, see Carvalho et al. (2009), for example. They obtained the mean void fraction by measuring the pulse-echo energy attenuation. It was particularly useful to identify flow pattern changes from bubbly to intermittent flows. They noted that bubbles can reflect considerably the emitted pulse. Figure 12 illustrates pulse-echo energy attenuation induced by dispersed bubbles.

Figure 12 – Illustration of pulse-echo energy attenuation induced by dispersed bubbles.

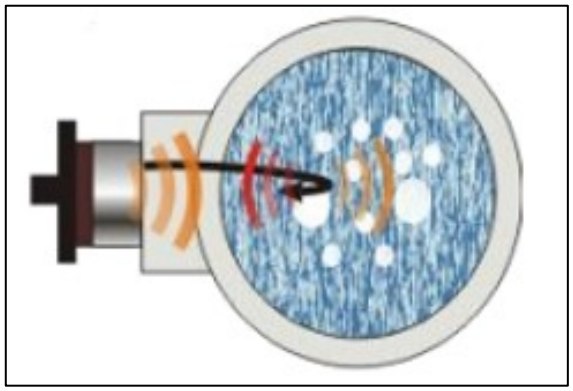

Source: Adapted, Ofuchi, C. Y. (2011).

### 2.4.4 Acoustic wave propagation mode: Shear waves

Wave propagation modes are related to the way that particles dispersed in a medium oscillate during energy transport. Shear waves are characterized by horizontally polarized waves with a large amount of energy. These waves describe the earth's seismological behavior during earthquakes (ROSE, 1999). Shear waves are commonly used when the material under analysis is covered by another material layer with different physical and chemical characteristics. Figure 13 illustrates shear wave action in a given medium. It can be used in vertical multiphase flows because more liquid is present on the tube wall.

Figure 13 – Illustration of shear wave action in a given medium.

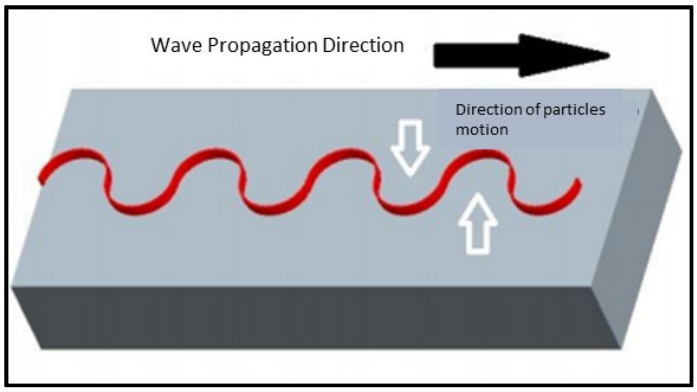


Source: Buenos (2010).

### 2.4.5 Multiphase Flow Measurements Using Ultrasonic Systems

Thorn, Johansen, and Hjertaker (2012) summarized flow measurement challenges in oil-gas-water mixtures at the oil and gas industry. They described measurement strategies and the most common applied technologies, including ultrasonic techniques.

Liang *et al*. (2016) developed a flow pattern identification method in two-phase horizontal gas-liquid flows. Their method focused on echo reflections from the inner pipe wall rather than the ones from the gas-liquid interfaces. It was observed that the reflection coefficient on wall-gas interfaces are more intense than on wall-liquid interfaces. They successfully identified stratified, annular and slug flow patterns.

Su, Tan, and Dong (2017) obtained the mean void fraction by measuring the pulse-echo energy attenuation in gas-liquid flows. They considered absorption and diffusion effects on wave energy attenuation. When the dispersed phase volumetric fraction is low, there is a closely linear relationship between the ultrasound attenuation coefficient and the volumetric phase fraction. Measuring difficulties were noted in flows with large void fractions.

Murakawa, Kikura, and Aritomi (2008) developed an ultrasonic technique for bubbly and slug flow patterns. To obtain liquid and gas velocity distributions ultrasonic transducers were employed. They applied piezoelectric elements in two working frequencies 2 and 8 MHz.

Murai *et al*. (2009) measured void fraction distributions in two-phase flows. Bubble interfaces were detected by the propagation of ultrasonic pulses in liquid along a measurement line. Both pulse-echo and Doppler methods were applied in signal processing. The void fraction profile was computed by the number of detected bubble interfaces.

Wada, Kikura, and Aritomi (2006) applied ultrasonic echo technique in air-water flows. Flow pattern identification was possible based on time delay and on changes of pulse-echo intensity. They also investigated the effects of solid plates made of acrylic and carbon steel on ultrasound transmission.

# 3 MATERIALS AND METHODS

## 3.1 EXPERIMENTAL SETUP

Figure 14 shows the schematics of the multiphase flow experimental setup, installed at UFSC in the Thermal Fluid Flow Group (T2F). Various flow configurations are possible, including mixtures of water, air and oil. Flow monitoring is possible owing to several sensors: absolute and differential pressure transducers, thermocouples, ECT tomography, a modified Venturi meter and ultrasonic sensors.

Figure 14 – Schematics of the multiphase flow experimental setup. Drawings are not in scale.

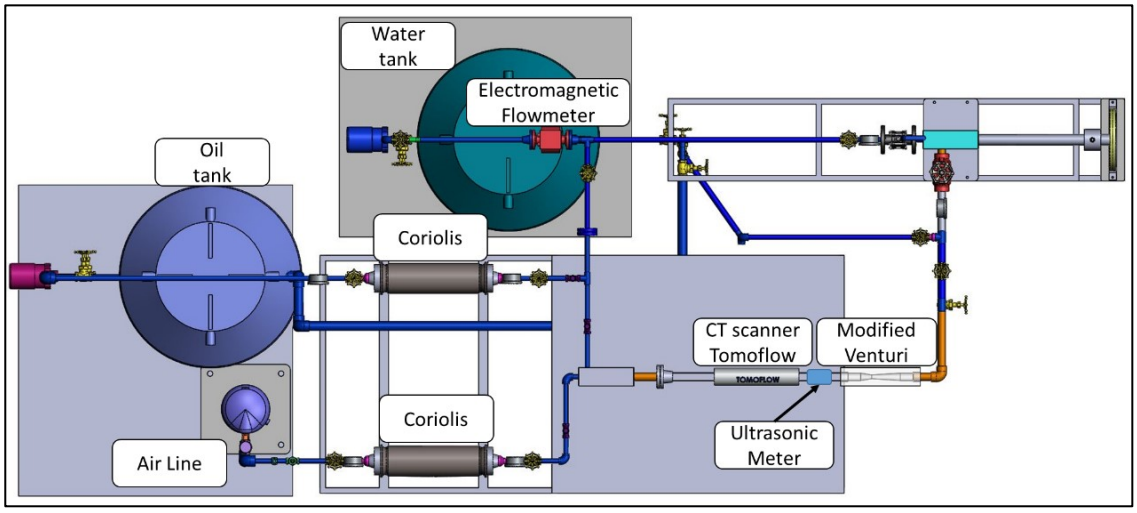


Source: Author (2020).

Air is provided by a SCHULTZ SRP-4025 compressor with static pressure equal to 6 bar. Filters, pressure and flow regulating valves allow fine-tuning control of the air inlet pressure. Air flowrate is obtained by a CFM200 Coriolis flowmeter. Working pressure was set in the range 0.1 to 2 bar, and measured by ROSEMOUNT absolute pressure sensors.

Water and oil flows are possible due to WEG BC-92S series centrifugal pumps. The in-line 2 kW pumps allow for maximum volumetric flow rates of 23.9 $m^3/h$. WEG-CFW500 frequency controllers and process valves permit fine-tuning of the mass flow rate of the flow in the measurement section. The water mass flow rate is measured by means of a Rosemount 8700M magnetic flowmeter, whose inaccuracy is less than 0.5% of the registered flow rate. The oil mass flow rate is measured by a CFM200 Coriolis flowmeter. Each water and oil reservoir contains about 0.35 $m^3$. This size facilitates temperature stabilization and hence

Reynolds number control. Thermocouples monitor working temperature in the flow loop. Tanks not shown in the figure above allow air-water-oil separation.

Air, water and oil lines present check valves in order to prevent backflow. In the present work, the test section consists of the flow segment where the ECT Tomoflow, the modified Venturi and ultrasonic sensors are located.

Signals from flowrate meters, absolute and differential pressure transducers, thermocouples and ECT tomography are routed via cables to National Instruments data acquisition systems. Data reading and processing are performed via software developed in LabVIEW platform. Figure 15 shows a photograph of the multiphase flow experimental setup.

Figure 15 - Photograph of the multiphase flow experimental setup.

Source: Author (2020).

### 3.1.1 Flow monitoring and Data Acquisition System

Flow monitoring was possible due to the following measuring instruments:

a) Absolute pressure transducers from DWYER Instruments, model 628-10-GH-P1-E1-S1;

b) ROSEMOUNT absolute pressure transducers from Emerson, model 2051TG3F2B21AB4E2M56;
c) Honeywell differential pressure transducers, TruStability ™ RSC model;
d) ROSEMOUNT Coriolis flowmeters from Emerson, model CMF200M418N0AMPZZZ;
e) KIMO Hot Wire Anemometer;
f) CT scanner ATOUT, Tomoflow PTL 300-TP-G model, with DAM200E-TP-G measuring system;
g) GE Panametrics Ultrasonic Flowmeter, Model PT868.

Table 2 shows the operating ranges, the uncertainties reported by the manufacturers and the number of measuring instruments. Expanded uncertainties are presented in the Annex A.

Table 2 – Characterization of flow monitoring instruments.

| **Measuring instrument** | **Operating range** | **Accuracy** | **Quantity** |
|---|---|---|---|
| Coriolis meter | 0 – 12.09 kg/s | ± 0.005 kg/s | 2 |
| Anemometer | 0.15 – 30 m/s | ± 0.05 m/s | 1 |
| DWYER absolute pressure sensor | 0 – 689000 Pa | ± 500 Pa | 2 |
| ROSEMOUNT absolute pressure sensor | 0 – 2e+6 Pa | ± 500 Pa | 2 |
| Honeywell differential pressure sensor | 0 – 30000 Pa | ± 1500 Pa | 2 |
| Honeywell differential pressure sensor | 0 – 60000 Pa | ± 3000 Pa | 2 |
| Honeywell differential pressure sensor | 0 – 90000Pa | ± 4500 Pa | 2 |

Source: Author (2020).

The CT scanner has two measuring planes separated by a distance of 460 mm, containing 12 electrodes each. More information will be presented in section 3.1.2. The ultrasonic flowmeter consists of two ultrasonic elements, working as senders and receivers. From the difference in the transit time, it is possible to measure average bulk velocity for single-phase flows. Further information will be presented in section 3.1.3.

Data acquisition and reading are obtained via NI-9203 current input module, NI-9214 thermocouple input module and CompactDAQ cDAQ-9178 chassis.

### 3.1.2 CT scanner

A Tomoflow PTL300E-TP-G sensor was used in order to measure two-phase flow statistics. The working principle is the difference in electrical permeability of each fluid. The transducer has two measuring planes with 12 electrodes per plane. Each electrode sends and receives electrical pulses as to determine the permeability. Through the DAM200E-TP-G measuring system and the ECT32 software, the Tomoflow sensor can provide two instantaneous cross-sectional views with the volumetric fractions of each phase. Cross-correlation of each measurement plane provides the velocity field.

Sensor calibration is necessary before measurements. Permeability of the each fluid is measured separately in accordance to the Process Tomography manual (2009). Figure 16 presents a schematics of the electrical capacitance principle used in Tomoflow PTL300E-TP-G.

Figure 16 - Schematics of the electrical capacitance signals processing used in Tomoflow PTL300E-TP-G.

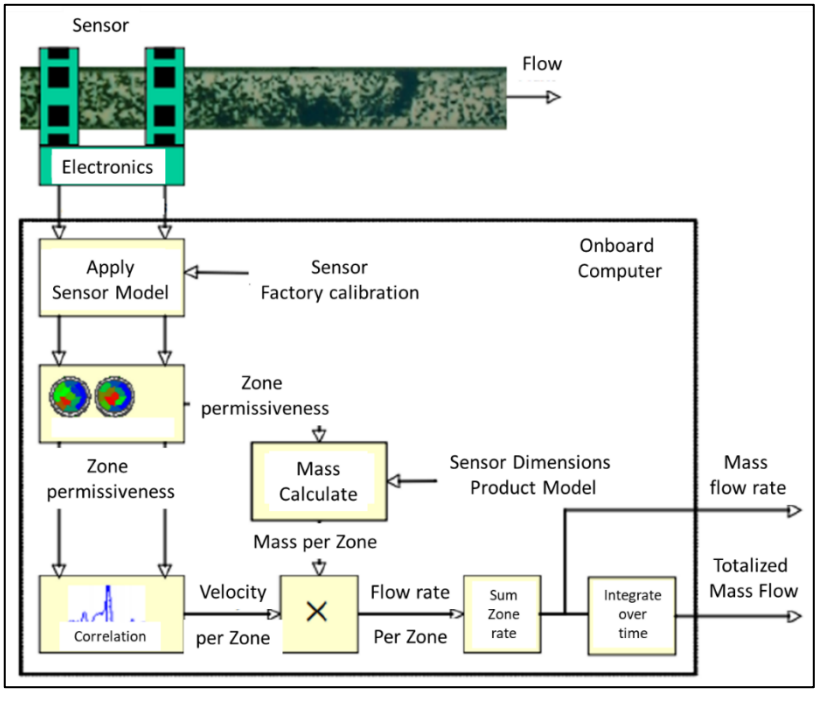


Source: Adapted from Process Tomography (2009).

Figure 17 shows an example of processing data on the ECT32 software screen. The red area represents the most permeable fluid, the blue area, the lowest permeable fluid. In-between colors indicate the presence of both fluids.

Figure 17 - Example of processing data on the ECT32 software screen.

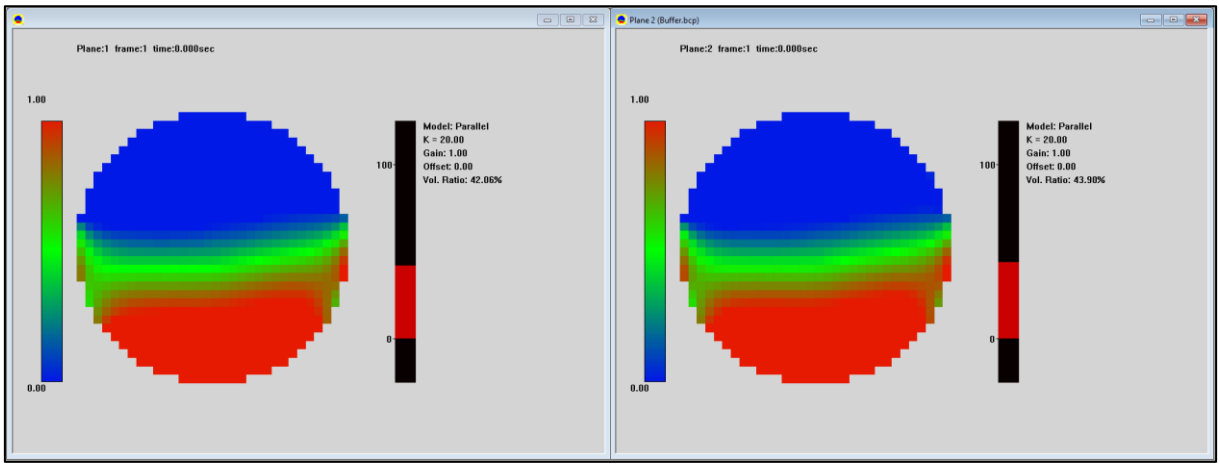


Source: Author (2020).

Data acquired by ECT32 are stored as .BCP files and processed by Flowan software. Cross-correlation technique is applied to determine the transit time of flow structures through a correlation peak. The first plan data is compared to the second plan data. With this information is possible to identify similar components in the flow and identify how the real behavior in the tube is. It is necessary to group pixels of the measurement system into zones of interest according to the analyzed flow pattern (TOMOFLOW LTD, 2003). The grouping of zones is called zone map. To categorize the zone maps Flowan uses permittivity information present in the data from ECT32. All this information is stored in a matrix and associates to the respective pixel that represents the tube. Figure 18 presents an example of zone map used in Flowan.

Figure 18 – Illustration of zone map created by Flowan software for stratified flow patterns.

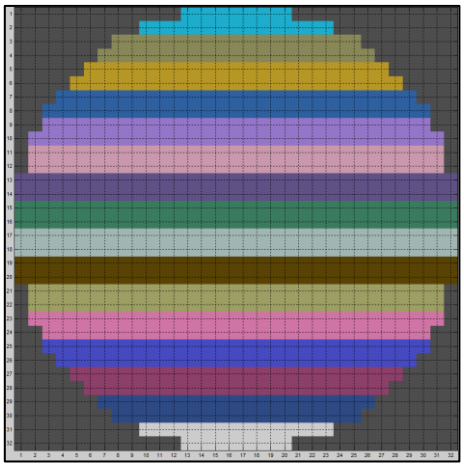

Source: Author (2020).

Cross-correlation $R_{\mathrm{xy,i}}$ in a given pixel "i" is calculated by means of the concentration $C_{1,i}$ at plane 1 and concentration $C_{2,i}$ at plane 2, (TOMOFLOW LTD, 2003):

$$R_{\mathrm{xy,i}}\ (\tau) = \lim_{T\to\infty} \int_0^T C_{1,i}(t).\, C_{2,i}(t+\tau)\, dt \tag{10}$$

where $T$ is the time window and $\tau$, the transit time of flow structures between the two planes. Although the correlation is described for averaging time T approaching infinity, in practice the user will need to set the window T at some suitable value appropriate to the particular velocity scales in the flow and the sensor geometry. The time delay at the peak of the correlogram corresponds to the transit time of flow structures between the two planes.

### 3.1.3 Ultrasonic Flowmeter

Although the GE Panametrics PT868 ultrasonic flowmeter has been designed for single-phase liquid flow measurements, it was applied in two-phase gas-liquid flows in the present work. It can measure bulk velocities from ± 0.03 to ± 12 m/s with an error of ± 0.005 m/s (PANAMETRICS, 1997). Figure 19 shows photographs of the applied sensors (a) and the acquisition system (b).

Figure 19 – Photographs of the applied flowmeter sensors (a) and the GE Panametrics PT868 signal acquisition system (b).

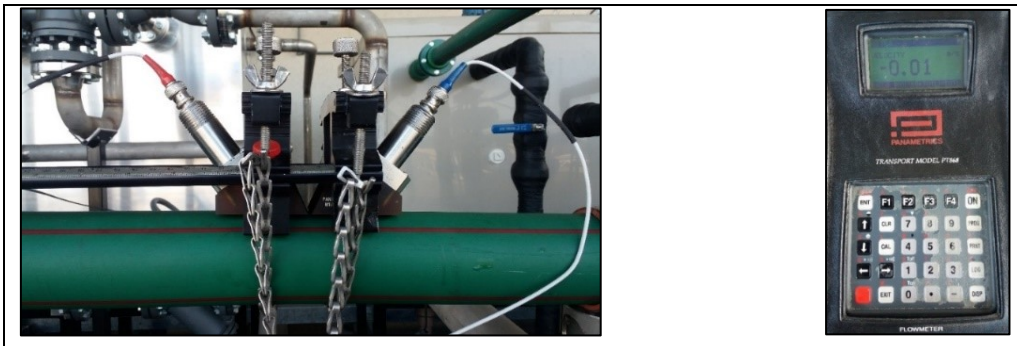


(a) (b)

Source: Author (2020).

#### 3.1.3.1 Flow cell

The flow cell uses ultrasonic pulses to measure the bulk flow velocity. It consists of a cell tube and transducers (PANAMETRICS, 1997). The cell tube can be mounted on an existing pipe or inserted as a section apart from the duct. It can be intrusive or fixed externally to the pipe by clamp-on fittings. It provides mechanical support to the transducers.

The transducers convert electrical energy into ultrasonic pulses in transmission cycles. They also convert ultrasonic pulses into electrical energy in reception cycles. Therefore, in the referenced system, they act as transmitters and receivers.

#### 3.1.3.2 Electronic components

The GE Panametrics PT868 ultrasonic flowmeter can convert electrical energy into ultrasonic pulses and ultrasonic pulses into electrical energy as a typical transmission-reception ultrasonic meter. To measure the transit time of ultrasonic pulses, the following components are necessary:

a) Signal Generator – it generates transmission signals and activates the transmitter;
b) Transmitter - it amplifies signals to the transmission transducer;
c) Receiver – it amplifies received signals to a suitable level to the data acquisition circuit;
d) Data acquisition circuit - it converts the signal to digital form and stores it in a buffer for microcontroller processing;
e) Time circuit – it determines the transmitter frequency, the transmission direction and the reception window, and controls the data acquisition circuit;
f) Microcontroller – it controls the flowmeter operation and calculates flow measurements based on received and transmitted signals. It also checks for failures and allows integrated troubleshooting diagnoses.

#### 3.1.3.3 Operation Theory

The meter uses the transit time of shear waves, transmitted through a moving liquid. The transit time is smaller if the pulses are applied along the main flow direction and longer if

applied in opposite direction. Bulk flow velocity computation is possible with the knowledge of the transit time, the distance between transducers, pipe material and pipe wall thickness. During the operation, each sensor sends and receives ultrasound pulses alternately. The number of transmitted and received pulses are identical. From these pulses, it is possible to measure the time interval between transmission and reception signals in both directions (PANAMETRICS, 1997). When the fluid velocity is zero, transit times are equal.

### 3.1.4 Modified Venturi Tube

A normalized Venturi tube, which follows ABNT NBR ISO 5167-1/1994 standard, has been applied in the test section. The meter is made of acrylic, allowing flow visualization. The ratio between the Venturi throat and the pipe inlet diameter, β, is 0.5. The inlet diameter is 40 mm and the throat diameter, 20 mm. A peculiar characteristic of this meter is the presence of six pressure measurement locations, besides the one at the pipe inlet. All holes were machined with inclination to the pipe axis in order to allow pressure drop measurements in gas-liquid flows. Bubbles hardly can enter into the pressure taps. The main goal of this meter design is to measure the static pressure evolution along the Venturi. Although it is not the aim of this thesis, a model will be developed to predict the theoretical pressure drop evolution as to predict mass flow rates of both liquid and gas streams. Figure 20 shows a side view schematics of the modified meter, including pressure drop locations.

Figure 20 - Side view schematics of the modified Venturi tube.

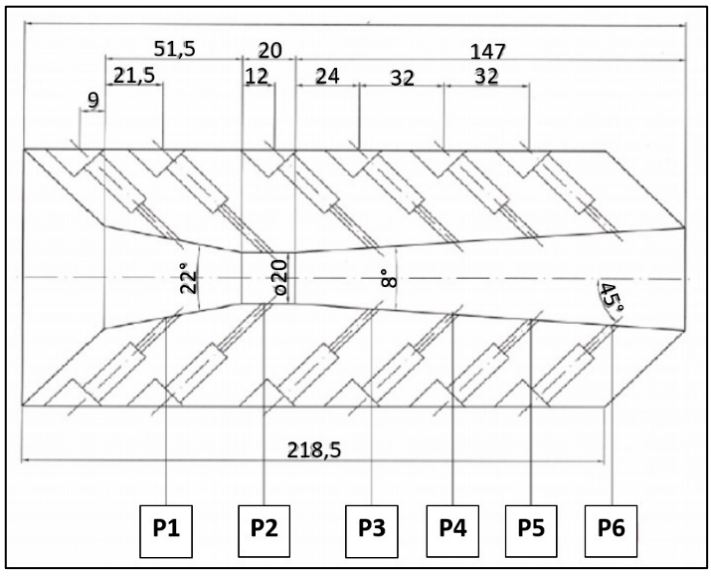


Source: Author (2020).

### 3.1.5 Crude Oil characterization

Ultrasound tests were performed in crude oil samples. Since crude oil properties are dependent on the well characteristics, laboratory experiments have been performed in order to obtain the sample mass density and its sound speed.

The average mass density was determined by averaging processes in accordance to Table 3. Five different volumes were tested. For each volume sample, mass was measured three times. The mean mass density including all experiments was 809.6 kg/m³.

Table 3 – Experimental determination of the crude oil mass density.

| Volume | | Mass | Mass density |
|---|---|---|---|
| [ml] | [mm³] | [kg] | [kg/m³] |
| 50 | 50000 | 0.040<br>0.039<br>0.041 | 800.0 |
| 75 | 75000 | 0.061<br>0.062<br>0.059 | 813.3 |
| 100 | 100000 | 0.083<br>0.080<br>0.083 | 820.0 |
| 125 | 125000 | 0.101<br>0.098<br>0.104 | 808.0 |
| 150 | 150000 | 0.122<br>0.121<br>0.120 | 806.7 |

Source: Author (2020).

The sound speed in a medium is given by:

$$c_{medium} = \sqrt{\frac{K}{\rho}} \tag{11}$$

where $c_{medium}$ is the sound speed in a medium, $\rho$, the mass density, and $K$, the bulk modulus of elasticity. For petroleum, $K$ ranges from 1.07e$^9$ to 1.49e$^9$ Pa (KINSLER *et al*., 1999). The sound speed of the applied crude oil lies between 1149.63 and 1356.62 m/s. The crude oil sound speed will be estimated in Chapter 4.

## 3.2 EXPERIMENTS

### 3.2.1 Data Acquisition

Experimental data has been obtained by both serial and wireless communication 2.4 GHz IEEE 802.15.4. Pressure drop data were transferred wireless. Two microcontroller boards were developed at UFSC, in the Software/hardware integration lab (LISHA), in order to transmit pressure drop data along the Venturi meter. An onboard microcontroller is responsible for data acquisition on the bench and send data to another one, with the same characteristics and connected to a personal computer. Data storage and reading are performed via a software developed in LabVIEW platform. Figure 21 presents a photograph of the software main screen and the Annex B presents the source code.

Figure 21 - Photograph of the software main screen with pressure drop measurements along the Venturi.


Source: Author (2020).

Mass flow rates, temperature and absolute pressure were obtained via USB serial communication. Pressure, temperature and flow rate data transmission occurred through an acquisition module of National Instruments CDaQ-9178. Data storage and reading are also performed via software in LabVIEW platform. Figure 22 presents a screenshot of the software main screen and the Annex C presents the source code.

Figure 22 - Screenshot of the software main screen with mass flow rates, temperature and absolute pressure measurements.

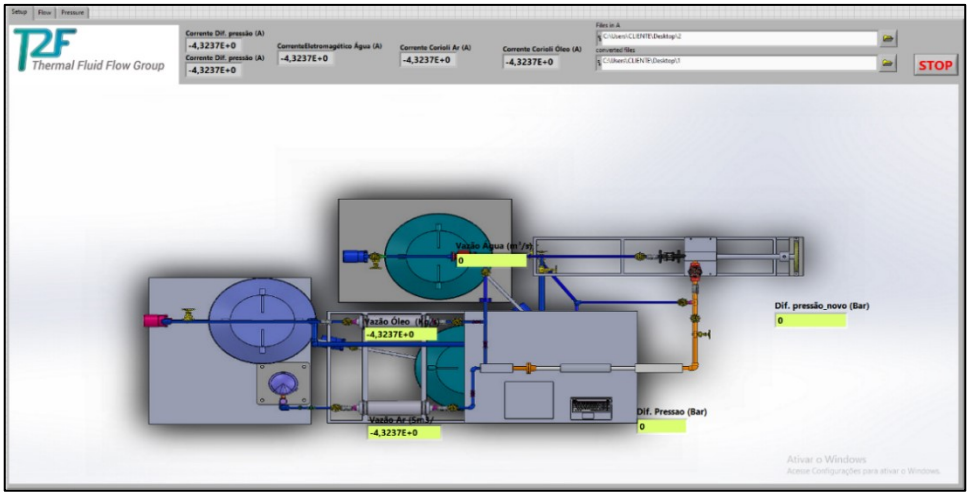


Source: Author (2020).

### 3.2.2 Concentration Measurements

Piezoelectric elements have been used to detect the interface between fluids in static columns and, therefore, determine volumetric concentrations. They were fixed on reservoir walls by a cyanoacrylate glue in order to avoid the air presence between the piezoelectric and wall surfaces.

The ultrasound method used in concentration tests was pulse-echo. The element working frequency was set to 1 MHz. The piezoelectric element worked as both emitter and receiver. Time of Flight (ToF) measurements have been registered in a personal computer via serial communication to further analysis. Figure 23 illustrates ToF measurements through a software in LabVIEW platform.

Figure 23 – Illustration of ToF measurements in LabVIEW platform.

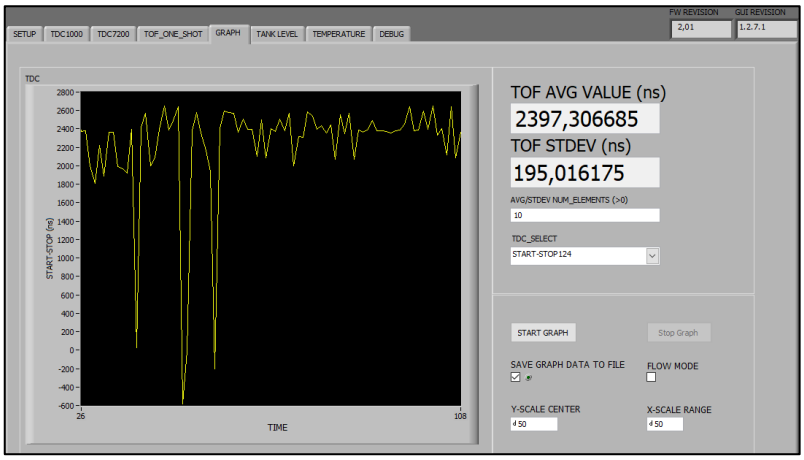


Source: Author (2020)

To determine the interface position by piezoelectric elements and ToF measurements, it is necessary to know the container dimensions. Measurements were made with two liquids (water and crude oil) and a gas (air) in a 125x125x125 $mm^3$ stainless steel box. The piezo-element was fixed at the case bottom; see a photograph of the experimental setup in Figure 24. Air is present in the case top. The following combinations were tested: water-air, crude oil-air and water-crude oil-air. Tests were made with the environment temperature set to 23 °C.

Figure 24 - Photograph of the experimental setup for concentration measurements in static columns.

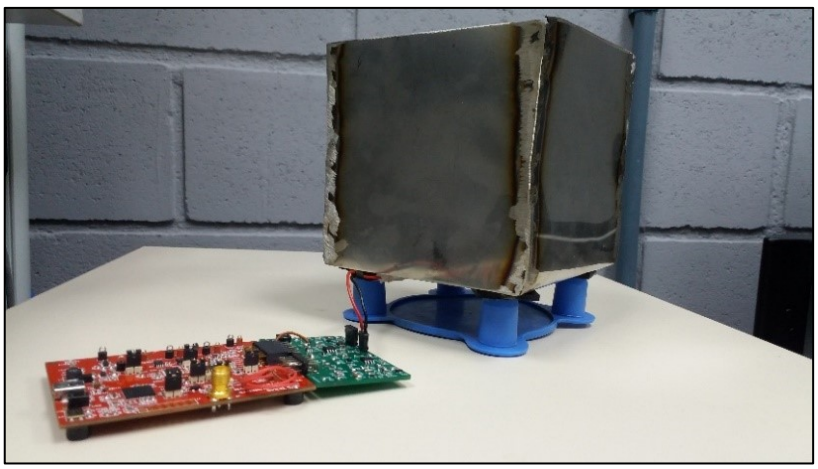

Source: Author (2020)

ToF measurements in water-air mixtures were performed with the maximum liquid column height equal to 95 mm. In crude oil-air mixtures, the maximum column height was

equal to 65 mm. ToF tests were executed in discrete steps of 5 mm until the maximum liquid column height was achieved. Column height measurements were executed with a DIGIMESS caliper whose uncertainty is ±0.025 mm. Results will be shown in the next chapter.

Throughout the concentration measurements, a piezoelectric element is excited with 5 V in order to generate ultrasonic waves. A TDC1000-TDC7200 EVM board from Texas Instruments was employed. The TDC1000 board was configured to control ultrasonic emission and reception from the piezoelectric element, measuring the elapsed ToF between START and STOP pulses.

Figure 25 shows the TDC1000 block diagram. An analog-front-end IC drives ultrasonic transducers in sensing applications. TDC1000 advantages include flexible programming and low power consumption. Multiple transmission pulses, signal thresholds and gain can be adjusted to allow measurements in several applications and systems with varying tank or pipe sizes.

Figure 25 - TDC1000 block diagram.

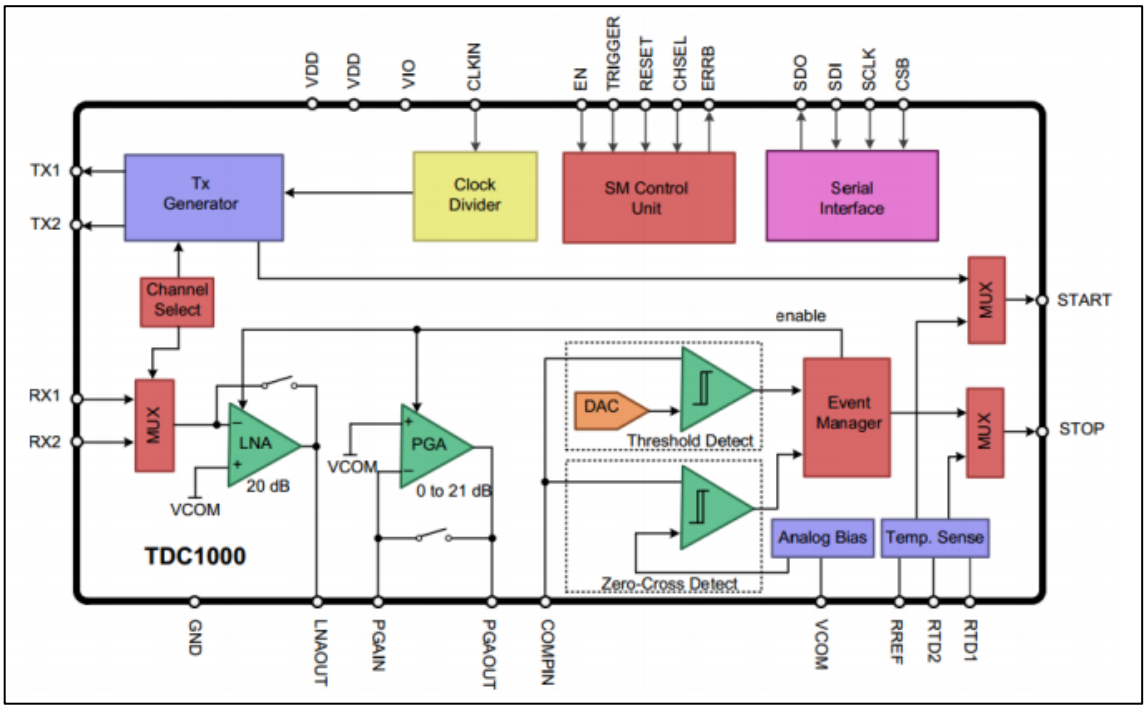


Source: LE (2015).

Figure 26 shows the TDC7200 block diagram, a time-to-digital converter with accuracy levels in picosecond range.

Figure 26 - TDC7200 block diagram.

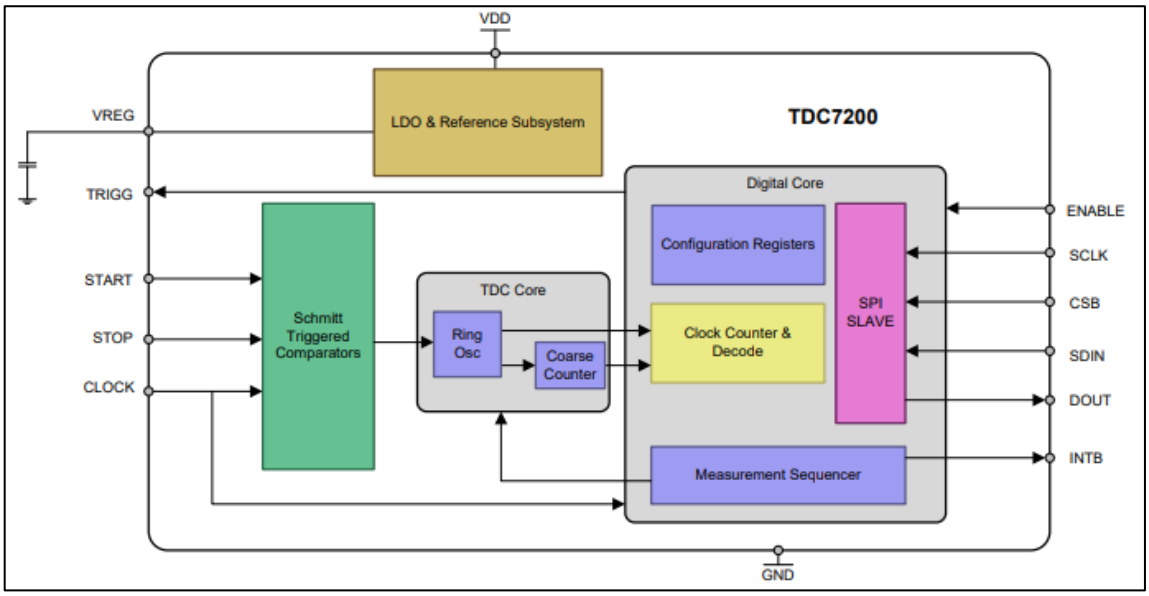


Source: LE (2015).

Figure 27 shows the TDC1000 configuration applied in the present work. The system was configured with two emission pulses and a single stop pulse. The threshold to identify the stop pulse is adjusted to -125 mV. PGA gain was set in 9 dB.

Figure 27 - TDC1000 configuration applied in the present work.

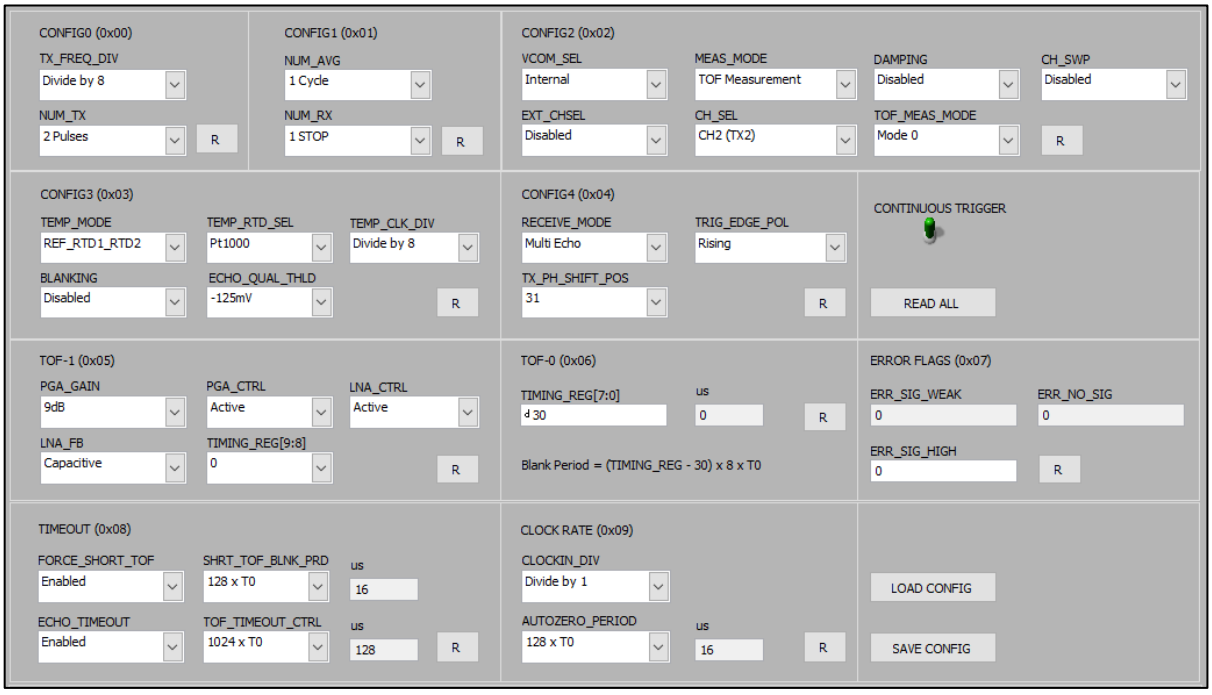


Source: Author (2020).

The volumetric fractions of water-crude oil mixtures can be determined with the measuring system calibration and the knowledge of the total liquid column height, $h$. Calibration is necessary to account for the effects of the glue and pipe walls on ToF measurements, and the emulsion spatial arrangement. With ToF measurements and the sound speed of each fluid, the water volumetric fraction, $\varsigma'$, can be obtained by:

$$\varsigma' = \frac{\left(\frac{2h}{ToF}\right) - Vs_{oil}}{Vs_{H_2O} - Vs_{oil}} \tag{12}$$

where $Vs_{oil}$ is the crude oil sound speed and $Vs_{H_2O}$, the water sound speed. In the present work, $Vs_{H_2O}$ was 1484.00 m/s. Three values were applied to $Vs_{oil}$ (1149.63, 1253.125 and 1356.62 m/s), since the crude oil properties were unclear. Crude oil concentration is given by 1 - $\varsigma'$. For water-crude oil-air mixtures, knowledge of the air column is necessary. The latter could be determined by ultrasound measurements at the gas-liquid interface if the emulsion and gas are separated.

### 3.2.3 Flow Rate Measurements

#### 3.2.3.1 Single-phase Flows

Fifteen single-phase flow experiments were performed with the GE Panametrics PT868 transmission-reception ultrasonic flowmeter and with the modified Venturi tube. Tap water with a controlled temperature was applied as working fluid. The water flows ranged from 0.70 to 2.10 kg/s. Results were compared to the ones provided by the Coriolis meter.

Tests were performed in horizontal and vertical directions. In horizontal direction, the flow reaches the Venturi and the ultrasonic meters after crossing nearly 50 pipe diameters without cross-section disturbances. Therefore, a fully developed flow can be assumed. The effect of flow disturbances on Coriolis meters are minor; see Kutin *et al*. (2006), for example. Due to changes in the experimental setup, tests in vertical direction were possible. Only ultrasound measurements were performed after the flow crossed 15 pipe diameters without disturbances upstream a 90º bend; see Figure 28. Therefore, flow disturbances were expected.

Figure 28 – Photograph of the experimental setup, showing setup changes to allow tests in vertical direction.

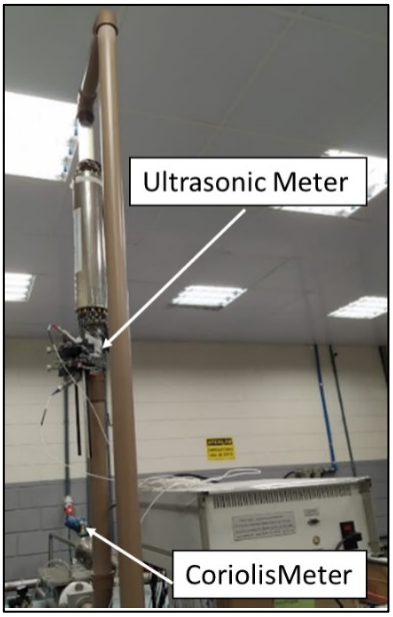


Source: Author (2020).

The mass flow rate was obtained with the Venturi meter as follows. Rearranging the Bernoulli, continuity and energy equations, and introducing the discharge coefficient, $C_d$, to account for dissipation effects, it is possible to correlate the Venturi mass flow rate, $m_v$, to the pressure drop in the throat, $\Delta p$, (OLIVEIRA *et al*., 2009):

$$m_v = \frac{C_d A Y F_a}{\sqrt{1-\beta^4}} \sqrt{2\rho\Delta p} \tag{14}$$

where $A$ represents the Venturi throat area, $\beta$ the throat to pipe diameter ratio, $\rho$ the mass density, $Y$ the compressibility coefficient, and $F_a$ the thermal expansion correction factor. Without thermal effects and considering an incompressible flow, $Y$ and $F_a$ are equal to one. $C_d$ is a function of the Reynolds number based on the bulk velocity and pipe diameter, $Re_D$. For $Re_D > 20000$, $C_d$ is nearly 0.98.

Pressure drop measurements were also measured in discrete points along the Venturi. Six differential pressure measurements in relation to the Venturi inlet occurred. These measurements allows the comparison between pressure drop models in converging-diverging cross-sections and experimental results. Cheap differential pressure sensors from Honeywell brand were integrated to an instrumented board as shown in Figure 31. The full scale of each

sensor was selected according to its position along the Venturi. Of course, the sensor scale close to the throat is bigger; see Table 2 in section 3.1.1. Pressure drop data were transmitted wireless; see section 3.2.1. Figure 29 shows a photograph of the pressure drop acquisition board.

Figure 29 - Photograph of the pressure drop acquisition board.

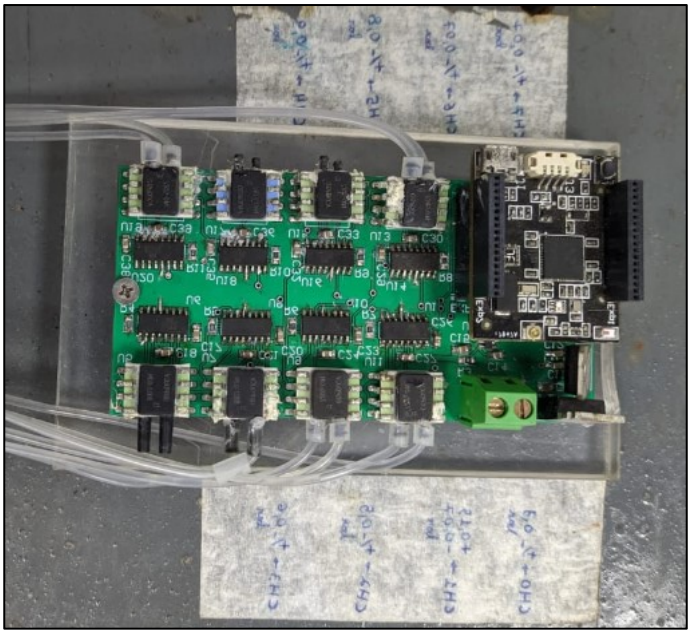

Source: Author (2020).

The mass flow rate was also obtained with the Ultrasonic meter as follows. With the mean bulk velocity measured by this meter, $v$, and the water mass density obtained by an equation of state dependent on temperature and absolute pressure measurements, the ultrasound mass flow rate, $m_{U.S.}$, is given by:

$$m_{U.S.} = \rho_l v A` \tag{15}$$

where $A`$ is the pipe cross-section area.

3.2.3.2 Two-phase Flows

Two-phase flows were evaluated with the GE Panametrics ultrasonic flowmeter, the modified Venturi tube and the ECT Tomoflow PTL300E-TP-G. It was evaluated the effect of

void fraction on liquid mass flow rate measurements for each meter. Water mass flow rates obtained by the Coriolis meter served as reference measurements. The void fraction ranged from 0.05 to 0.63. Three different flow patterns were investigated: bubbly, slug and stratified patterns in horizontal flow direction. The limiting void fractions for measurements in horizontal and vertical directions were determined for the ultrasonic flowmeter.

Coriolis meters were installed in each water and air lines. The Coriolis measurement range for airflows was oversized for the applied air mass flowrates. As an alternative to determine the air mass flow rate in two-phase flows, an anemometer was used in the air line. The air mass flowrates, $m_{air}$, were obtained with the equations below:

$$\rho_g = \frac{p+101325}{287.0856(273+temp)} \tag{16}$$

$$m_{air} = \rho_g v A` \tag{17}$$

where $\rho_g$ stands for the air mass density and it is calculated using ideal gas law, $p$ the absolute pressure [Pa], $temp$ temperature [°C], $v$ mean bulk velocity, and $A`$ the pipe cross-section area.

Quality and mean void fraction are given by:

$$x = \frac{m_{air}}{m_{air}+m_{coriolis}} \tag{18}$$

$$\alpha = \frac{1}{\left(\frac{\rho_g}{\rho_l} S \frac{1-x}{x}\right)+1} \tag{19}$$

where $m_{coliolis}$ is the water mass flow rate, $\rho_l$ the water mass density (kg/m³) and $S$ the mean slip ratio. The mean slip ratio can be roughly approximated to 1 in bubbly flows or low void fractions. OLIVEIRA *et al*., 2009 obtained mean slip ratios in the range 1-2 for bubbly and plug patterns in gas-liquid flows and for mean void fractions less than 0.7. Only for churn and annular patterns and mean void fractions over 0.7, the mean slip ratio surpassed this reference.

Measurements were also obtained by the CT scanner. Although the CT spatial resolution was poor to characterize bubbly flows with bubbles less than 1 mm, it was sufficient to characterize slug and stratified patterns. However, the informed mean

concentrations obtained by the CT scanner in bubbly patterns match the ones obtained with Eq. (19) and $S$=1. Figure 30 shows instantaneous tomographic images of bubbly, slug and stratified patterns, respectively. Cross-section images stand for permittivity average within the measurement volume surrounding the electrodes. The red area represents water, the blue area, air. In-between colors indicate presence of both fluids.

Figure 30 – Tomographic cross-section images of bubbly, slug and stratified patterns.

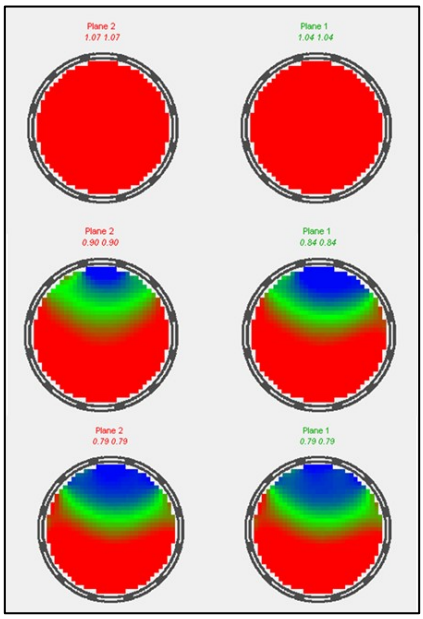


Source: Author (2020).

### 3.2.4 Flow pattern identification

Flow pattern identification was achieved by applying Fast Fourier Transform (FFT) in pressure drop signals along the Venturi tube and in the mean concentration signals obtained by the CT scanner. The same patterns were investigated: bubbly, slug and stratified patterns in horizontal flow direction. Similar boundary conditions as presented in the previous section were applied.

#### 3.2.4.1 Pressure drop signal

Fast Fourier Transform (FFT) was applied to pressure drop signals along the Venturi tube. The method analysis consisted of applying filters to select frequencies with higher amplitude content. In order to apply FFT, high measurement frequencies are needed.

Measuring frequency adjusted to 60 Hz was sufficient at the present work. Of course, only the dynamic amplitude content was analyzed: the instantaneous signal is subtracted from the ensemble average in each measurement point. The identification analysis also included statistical tools such as the mean and the mean standard deviation.

### 3.2.4.2 Concentration signal

The following procedure was necessary to apply FFT to concentration signals. Files with water concentration data were generated using the Flowan software provided by the CT equipment. The CT scanner provides flow images in two planes via ECT32 software. These images are saved in BCP format where measuring information is sorted out in maps. Flowan recreates cross-section images from the BCP files, the flow info and the CT scanner configuration. Figure 31 shows an illustration of Flowan main screen with cross-section images and concentration signals in a given time span. The concentration signal can be exported for further analysis.

Figure 31 - Illustration of Flowan main screen with cross-section images and concentration signals in a given time span.

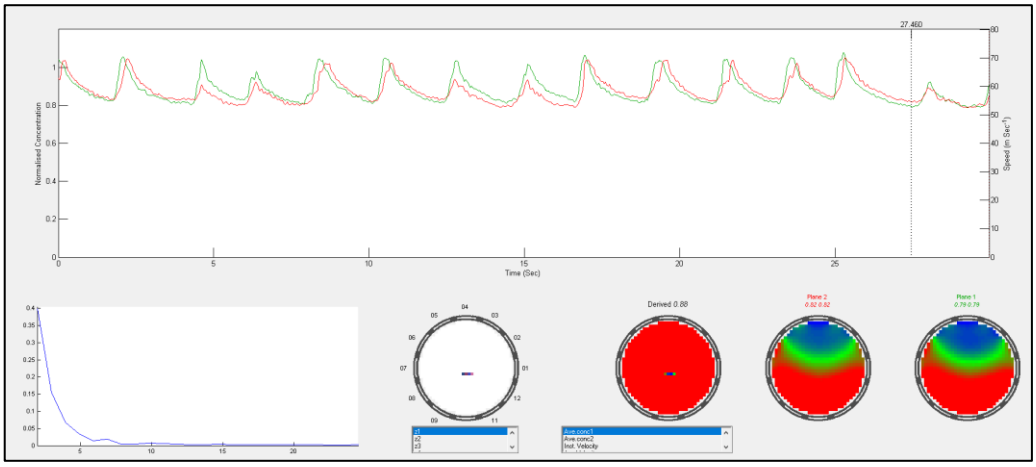

Source: Author (2020).

Data can be exported from 32 areas within the pipe cross-section at two different planes. Each area consists of 38 pixels and, therefore, each cross-section plane consists of 1216 pixels. The instantaneous mean concentration in a plane is a data average of all 1216 pixels.

Analysis of the mean concentration signal is similar to the one presented above. The instantaneous signal is subtracted from the ensemble average with the aim of applying the FFT. This filtrate all the information that surrounds the origin to analyze the dynamic amplitude content. The identification analysis also includes statistical tools such as the mean and the mean standard deviation.

# 4 RESULTS

## 4.1 STATIC MEASUTEMENTS

### 4.1.1 Boosting Transmission Pulses

To enhance the piezoelectric capability of obtaining the echo response, the energy content in the transmission pulse must increase if compared to the ones in usual commercial pulses. This necessity is also observed when the medium is mostly in gaseous phase, typical of wet gas production.

A commercial TDC1000-BSTEVM board was directly connected to a PCB boost board to increase the ultrasound transmission pulse energy. The ultrasound sensors are usually fed by a 3.7 V source with this board. To have a large amplitude the boost board feed the ultrasound sensors by a 30 V source. Figure 32 shows the schematics to boost the source power of ultrasound sensors. Figure 33 shows the design of the PCB boost board.

Figure 32 - Schematics to boost the source power of ultrasound sensors.

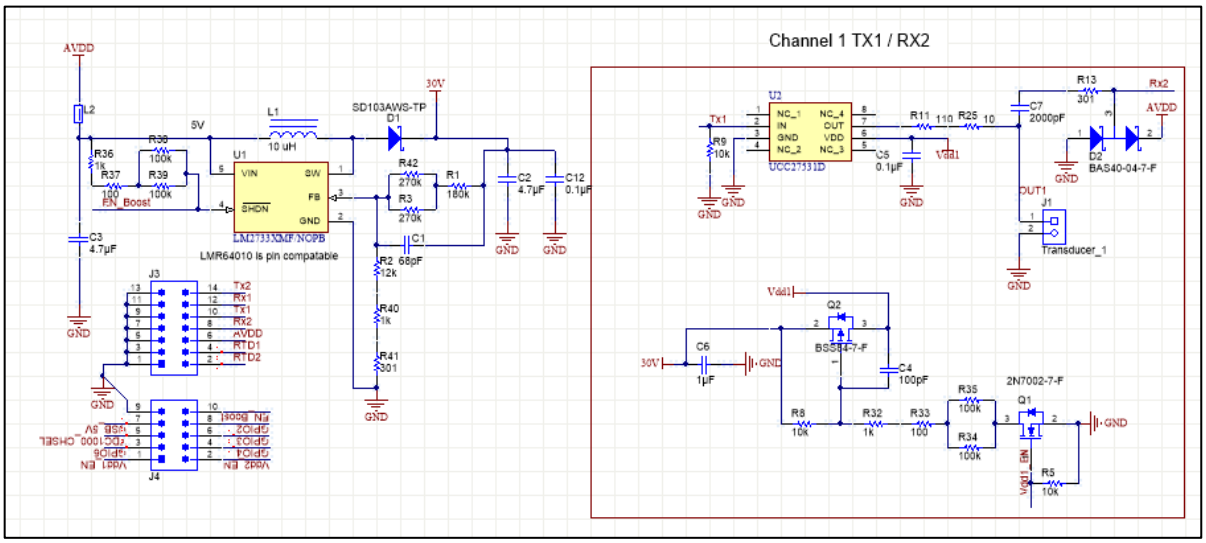


Source: Author (2020).

Figure 33 – Design of the PCB boost board.

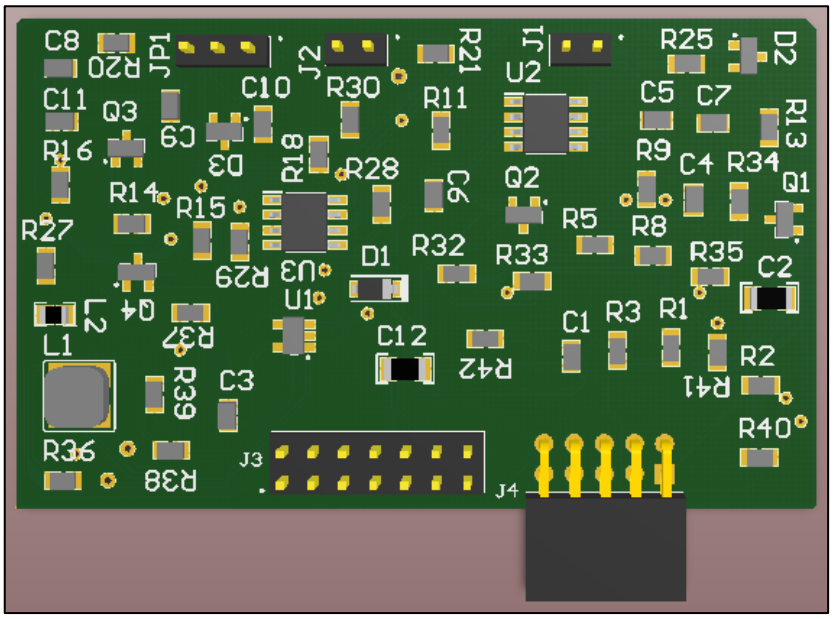


Source: Author (2020).

### 4.1.2 Concentration Measurements

Figure 34 shows the effect of the water column height on pulse-echo concentration measurements in water-air static columns. ToF tests were executed in discrete steps of 5 mm until the liquid column height was equal to 95 mm. Echo measurements were adequate for measuring heights over 15 mm. This occurs because the piezoelectric elements do not have a sensibility to identify these changes in the heights. Pulse-echo concentration results match the experimental results within measurement uncertainty. Error-bar sizes varied between 1.8 and 4.9 mm. Uncertainties were computed accordingly to the Annex A in 95% confidence intervals.

Figure 34 - Effect of the water column height on pulse-echo concentration measurements in static columns with water and air.

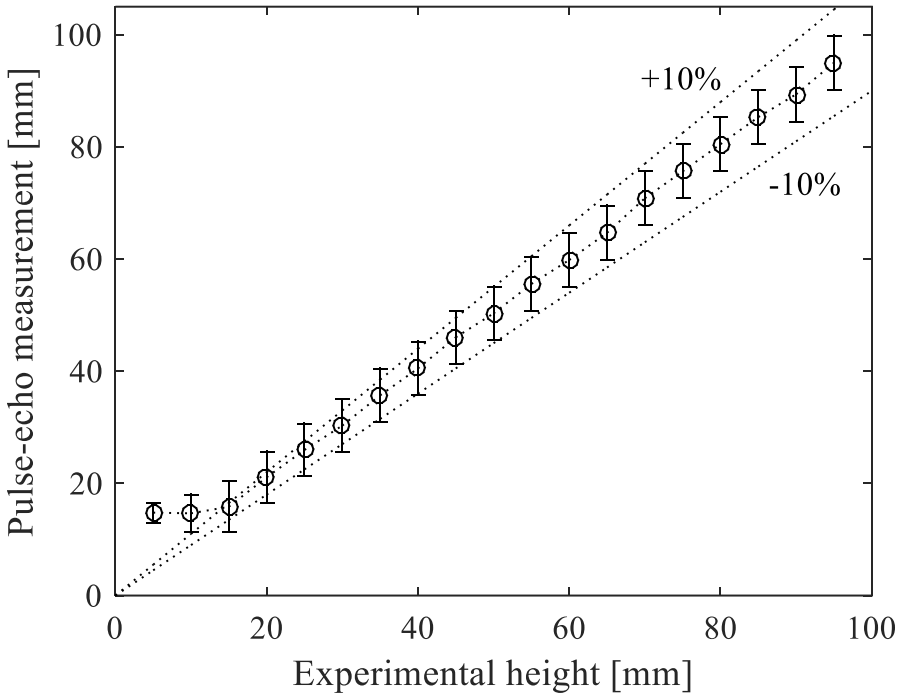


Source: Author (2020).

Figure 35 shows the effect of the crude oil column height on pulse-echo concentration measurements in static columns with crude oil and air. ToF tests were executed in discrete steps of 5 mm until the liquid column height was equal to 65 mm. Since the precise value of the crude oil sound speed is unclear, three $c_{medium}$ values were tested in accordance to section 3.1.5: 1149.63, 1253.12 and 1356.62 m/s. Pulse-echo concentration results corresponded to the experimental values if $c_{medium}$ = 1356.62 m/s. Echo measurements were satisfactory for measuring heights over 10 mm. Error-bar sizes varied between 0.7 and 1.1 mm. The same measuring system applied to static columns with water and air can be applied to columns with crude oil and air.

Figure 35 - Effect of the crude oil column height on pulse-echo concentration measurements in static columns with crude oil and air.

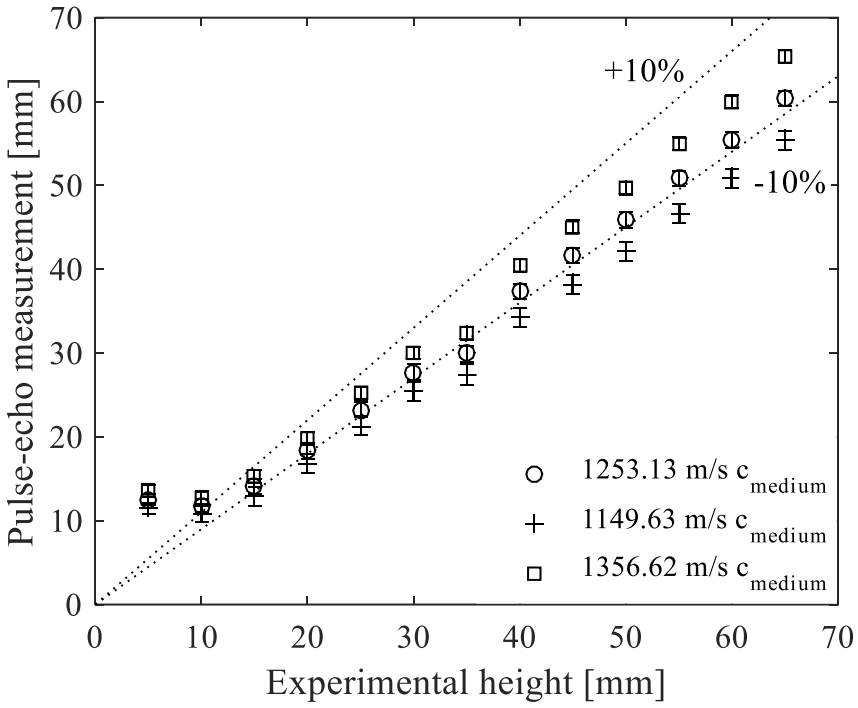


Source: Author (2020).

Figure 36 shows the effect of the crude oil and water column heights on pulse-echo concentration measurements in static columns with water, crude oil and air. Eleven ToF tests were executed with the liquid column (water and oil) height in the range 20 -85 mm. The columns of liquid were distributed with water at the bottom with a crude oil column above it and an ambient air column above them. The water column starts with 20 mm height and alternating crude oil and water are added at each 5 mm. Once again, three values of crude oil sound speed were tested: 1149.63, 1253.12 and 1356.62 m/s. Echo measurements were satisfactory for measuring heights over 20 mm. Pulse-echo crude oil and water mean concentration results match the experimental results within measurement uncertainty with ± 10% of the expected value. Error-bar sizes varied between 1.0 and 9.4 mm. These values stand for crude oil and water mean concentration uncertainties equal to 0.0533 and 0.1882, respectively. Note that crude oil sound speed variations slightly affected the concentration estimations with pulse-echo tests in static columns with water, crude oil and air. The same measuring system applied to water-air and crude oil-air static columns can be applied to water-crude oil-air static columns.

Figure 36 - Effect of crude oil and water column heights on pulse-echo concentration measurements in water-crude oil-air static columns.

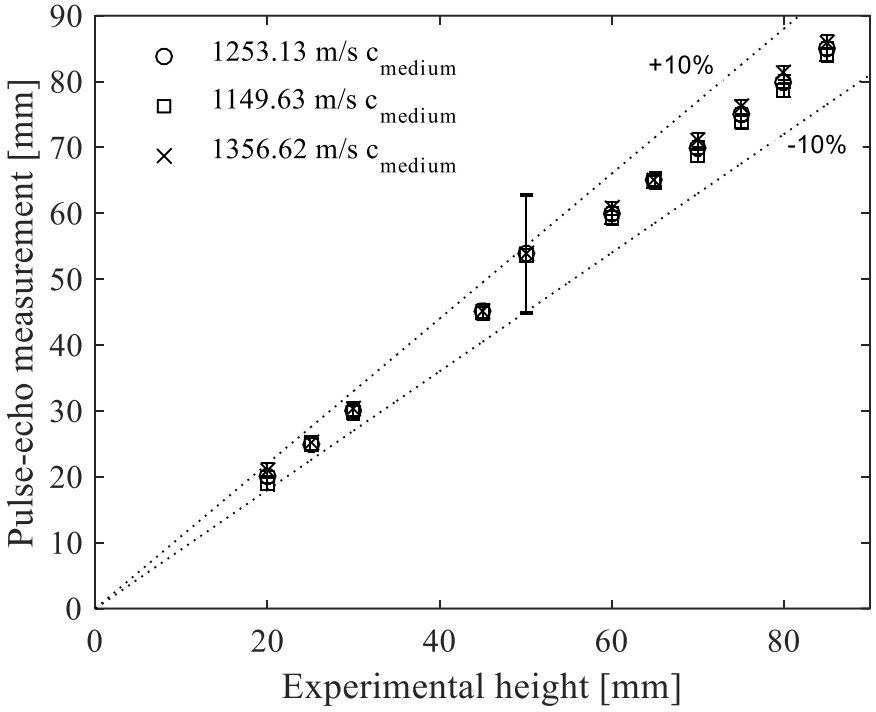


Source: Author (2020).

## 4.2 DYNAMIC MEASUREMENTS

Figure 37 shows a summary of all two-phase experimental points. The air mass flow rate is plotted as a function of the mean void fraction assuming that $S = 1$. Dotted, dot-dashed and straight tendency lines were added to identify the measured flow patterns. All flow patterns were identified by eye. Symbols stand for experiments with the same water flow rate. Inlet pressure ranged from 0.036 to 2.05 bar at environment temperature of 23 $^{o}$C. Note that different flow patterns may occur with the same mean void fraction.

Figure 37 - Summary of all two-phase experimental points. Dotted, dot-dashed and straight tendency lines stand for bubbly, slug and stratified patterns in horizontal flows.

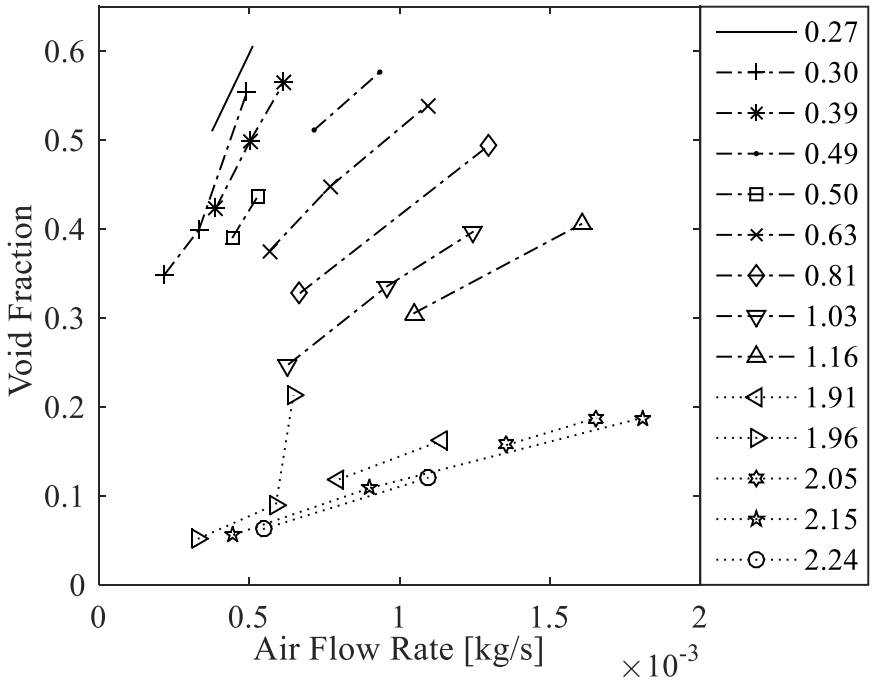


Source: Author (2020).

### 4.2.1 Mass Flow Rate Measurements

4.2.1.1 Single-phase flows

Figure 38 shows single-phase mass flow rate measurements in horizontal flow direction for the Venturi tube and the transmission-reception ultrasound. Water flow rates ranged from 0.70 to 2.30 kg/s. The Coriolis meter provided measurements with an accuracy of ± 0.005 kg/s and therefore served as a reference meter. Both meters showed measurements errors less than ± 10% relative to the reference values.

Figure 38 - Single-phase mass flow rate measurements in horizontal flow direction.

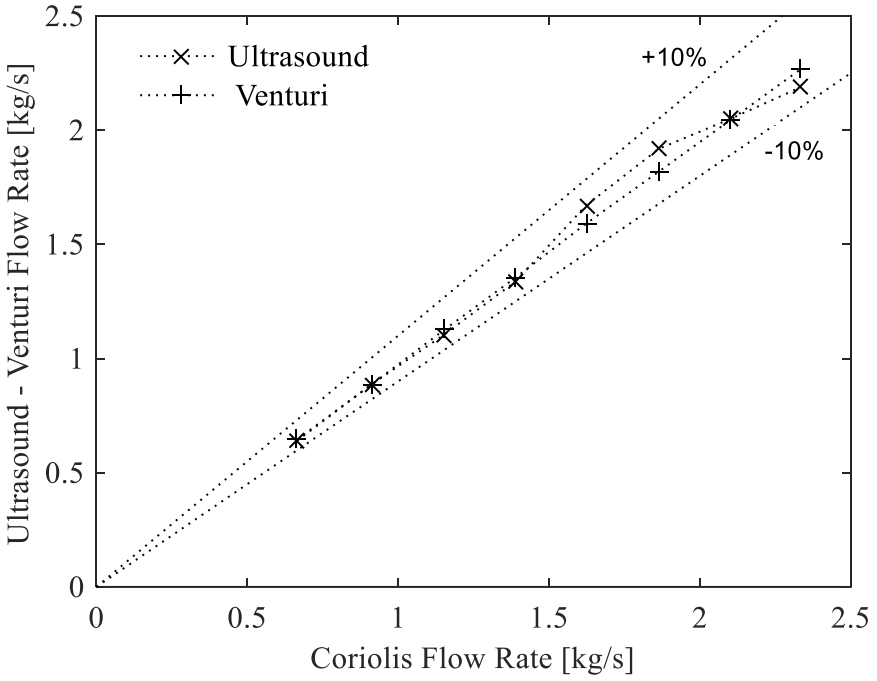


Source: Author (2020).

Uncertainties for the Venturi meter varied between 0.0101 and 0.0356 kg/s. For the Ultrasonic meter, uncertainties were nearly 0.02 kg/s. The good agreement between the experimental results confirms that the flow can be considered fully developed in horizontal direction.

Figure 39 shows single-phase mass flow rate measurements in vertical flow direction for the transmission-reception ultrasound. Water flowrates also ranged from 0.70 to 2.30 kg/s. Ultrasound measurements matched the reference ones within measurement uncertainty, nearly 0.02 kg/s. The flow could not be considered fully developed, since the development occurred along only 15 pipe diameters downstream a 90º bend. Flow disturbances did not promote misleading errors.

Figure 39 - Single-phase mass flow rate measurements in vertical flow direction.

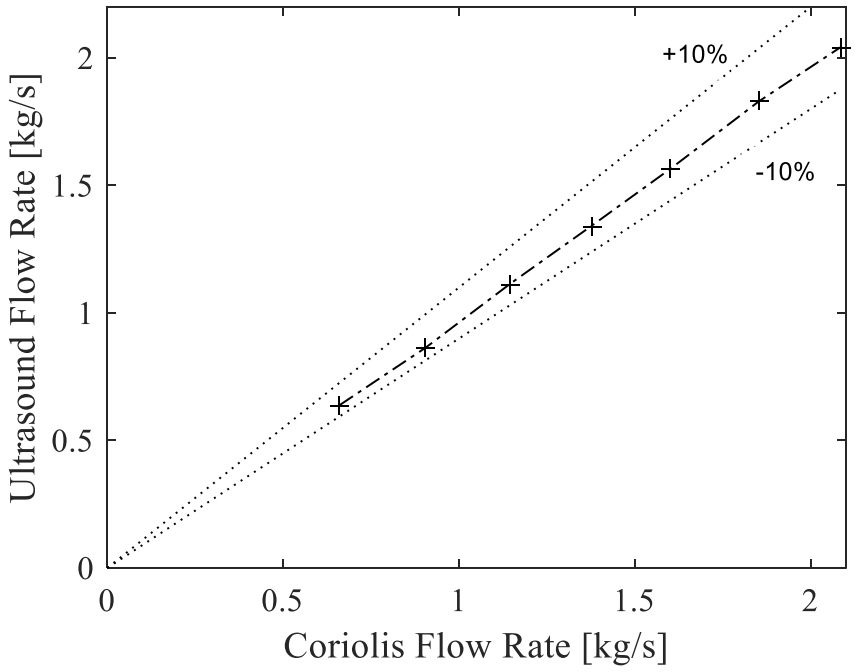


Source: Author (2020).

4.2.1.2 Two-phase flows

Figure 40 shows the effect of void fraction on liquid mass flowrate measurements for ultrasound and Venturi meters in horizontal and vertical gas-liquid flows. The data presented in blue refer to ultrasonic measurements in horizontal and vertical flows. These values were found using Equation 15 presented in Chapter 3 calculated using the velocity measured by the ultrasonic meter. The data presented in black refer to the Venturi meter measurements. These values were found using Equation 14 presented in Chapter 3. The correction values were calculated to adjust the Venturi tube measured curve and is calculated using Equation 20 presented in sequence. Also shows the effect of void fraction on liquid mass flowrate measurements for ultrasound meter in vertical gas-liquid flows. The void fraction experiments ranged from 0.03 to 0.62.

Figure 40 - Effect of void fraction on liquid mass flowrate measurements for ultrasound and Venturi meters in horizontal and vertical gas-liquid flows.

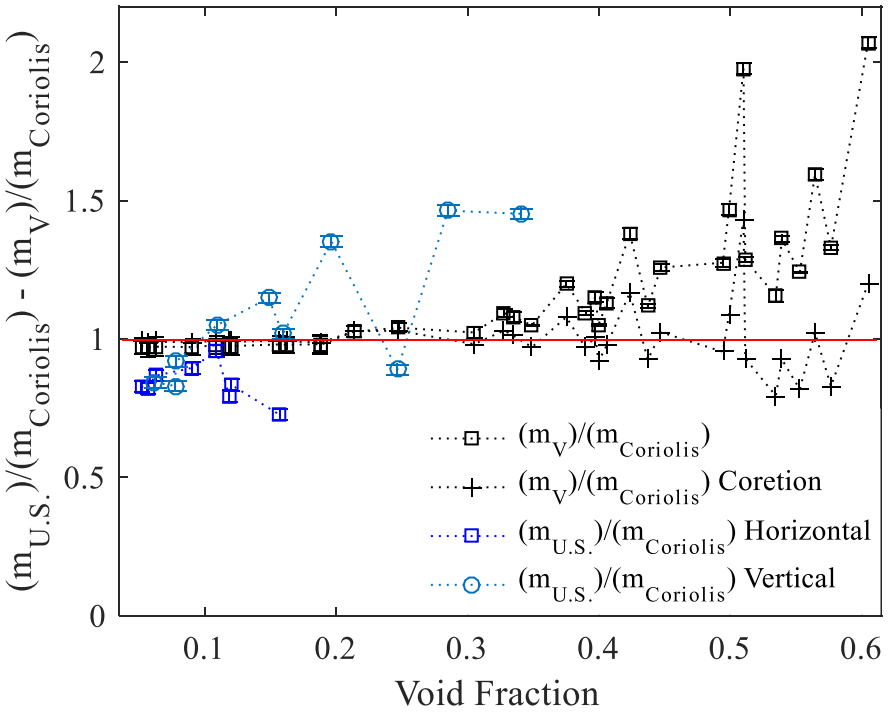


Source: Author (2020).

Venturi meter measurements overestimated the liquid mass flow rate for void fractions over 0.2 in the present working conditions. The water mass density was applied in the mass flow rate computation with the Venturi. It is well known that viscous dissipation effects increase in two-phase flows, causing higher pressure drop in the Venturi throat. This fact is often accounted for by two-phase friction factors which amplifies single-phase values. However, the pressure drop increase was minor for bubbly patterns and void fractions less than 0.2. One way of correcting the liquid mass flow rate is to consider correction functions based on mean void fraction measurements. In this case Venturi meter measurements overestimated the liquid mass flow rate for void fractions over 0.5 in the present working conditions. The correction function achieved to Venturi mass flow rate is:

$$m_{v.c.} = \frac{m_v}{(4.661\alpha^{3.654}+1)} \tag{20}$$

This equation is valid only to void fraction values below 0.63.

Ultrasound measurements underestimated the liquid mass flow rate in horizontal flow direction and mostly overestimated in vertical direction. Relative errors varied between 5

and 28% in horizontal flows, and between 2 and 46% in vertical flows. It was identified limiting working conditions: measurements were only possible for void fractions less than 0.18 in horizontal flows, and less than 0.32 in vertical flows.

Several issues can affect ultrasound mass flow rate measurements in gas-liquid flows: fluid properties, interfaces, gravity, among others. They are addressed as follows. Acoustic waves are affected by fluid properties, particularly the sound speed in the medium, which is nearly 335 m/s for air and 1484 m/s for water. The presence of air-water interfaces causes wave reflection and refractions all over the domain. Gravity modifies the distribution of phases affecting wave propagation, refraction and reflection. Furthermore, the bulk liquid velocity increases with increasing void fraction for two-phase flows with the same liquid mass flow rate.

The emission and reception sensors were adjusted for one traverse: it means that the acoustic emission wave is expected to achieve the pipe wall opposite to the emission location and then to be reflected towards the reception sensor. In horizontal flows, air is mostly concentrated in the upper part of the pipe cross-section. The wave energy content is highly reflected or refracted in this region, and with low mean void fractions (0.18, in the present work) the transmission signal is lost. In vertical flows, the phases are better distributed in the pipe cross-section. Only for mean void fractions over 0.32, the wave reflection/refraction is intense enough to cause signal interruption.

### 4.2.2 Pressure Drop Measurements along the Venturi Tube

#### 4.2.2.1 Single-phase flows

Figure 41 shows the effect of converging-diverging geometry on the pressure drop along the Venturi tube for water single-phase flows. A typical incompressible flow behavior is noted with static pressure recovery in the diverging geometry. The decrease in static pressure is subtle in the converging geometry and mainly occurs in the Venturi throat where the *vena contracta* is located. Tendency lines were added to guide the eye. The results below suggests a fully developed single-phase flow.

Figure 41 – Effect of converging-diverging geometry on the pressure drop along the Venturi tube for single-phase flows. Tendency lines were added to guide the eye. Water flowrate in kg/s.

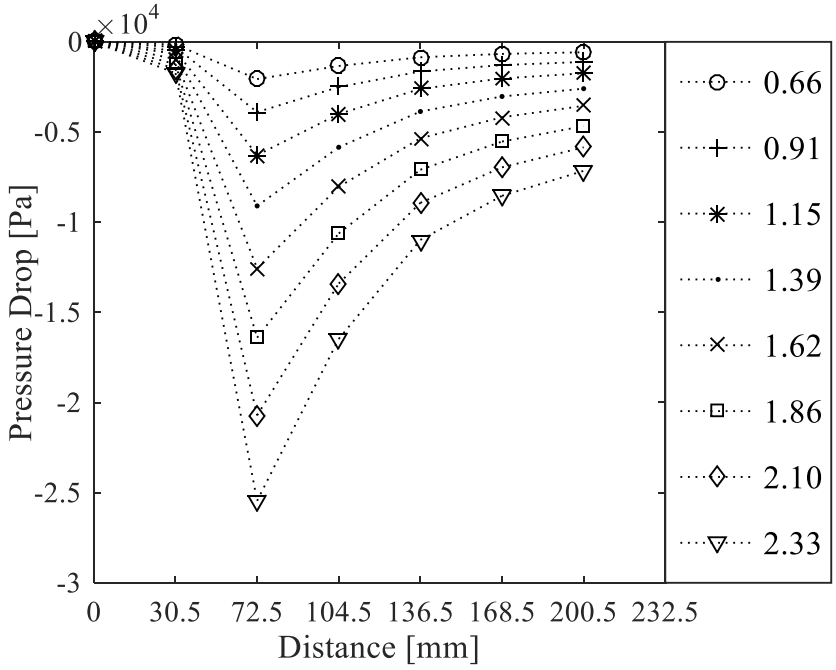


Source: Author (2020).

4.2.2.2 Two-phase flows

Figure 42 shows the effect of converging-diverging geometry on the pressure drop along the Venturi tube for bubbly flows. Tendency lines were added to guide the eye. A constant was added to every set of results to improve visualization. From the top to the bottom: +14000, +12000, +10000, +8000, +6000, +4000, +2000, +0, -2000, -4000, -6000. Results in Pa. Air mass flow rate ranged from 0.0003 to 0.0018 kg/s and water mass flow rate ranged from 1.9 to 2.26 kg/s. The mean void fraction ranged from 0.051 to 0.19. For bubbly patterns, the static pressure behavior is similar to the one observed in single-phase flows.

Figure 42 - Effect of converging-diverging geometry on the pressure drop along the Venturi tube for bubbly flows. Tendency lines were added to guide the eye. Water flowrate in kg/s. Air flow rate ranged from 0.0003 to 0.0018 kg/s. A constant was added to every set of results to improve visualization. From the top to the bottom: +14000, +12000, +10000, +8000, +6000, +4000, +2000, +0, -2000, -4000, -6000.

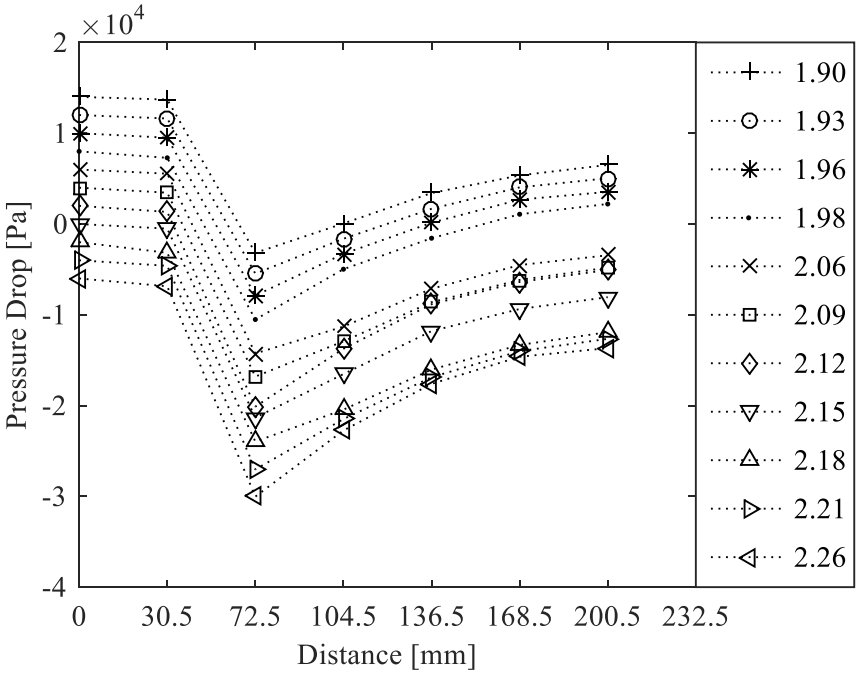


Source: Author (2020).

Figure 43 shows the effect of converging-diverging geometry on the pressure drop along the Venturi tube for slug flows. Tendency lines were added to guide the eye. A constant was added to every set of results to improve visualization. From the top to the bottom: +5000, +4000, +3000, +2000, +1000, +0, -1000, -2000, -3000, -4000, -5000, -6000. Results in Pa. Air mass flow rate ranged from 0.0004 to 0.0036 kg/s and water mass flow rate ranged from 0.49 to 1.26 kg/s. The mean void fraction ranged from 0.21 to 0.58.

For slug patterns, the static pressure behavior is slightly modified in relation to the ones shown in single-phase or bubbly flows. The static pressure was equal or increased in the converging geometry. The static pressure recovery in the diverging geometry was interrupted in the last part of the diverging zone. These results are explained as follows. For slug flows, the 90º bend positioned 5 pipe diameters downstream the Venturi outlet caused flow disturbances along the Venturi tube. It is also possible that compressibility effects took place. These remarks will be clearly noticed in the results for stratified patterns.

Figure 43 – Effect of converging-diverging geometry on the pressure drop along the Venturi tube for slug flows. Tendency lines were added to guide the eye. Water flowrate in kg/s. Air flow rate ranged from 0.0004 to 0.0036 kg/s. A constant was added to every set of results to improve visualization. From the top to the bottom: +5000, +4000, +3000, +2000, +1000, +0, -1000, -2000, -3000, -4000, -5000, -6000.

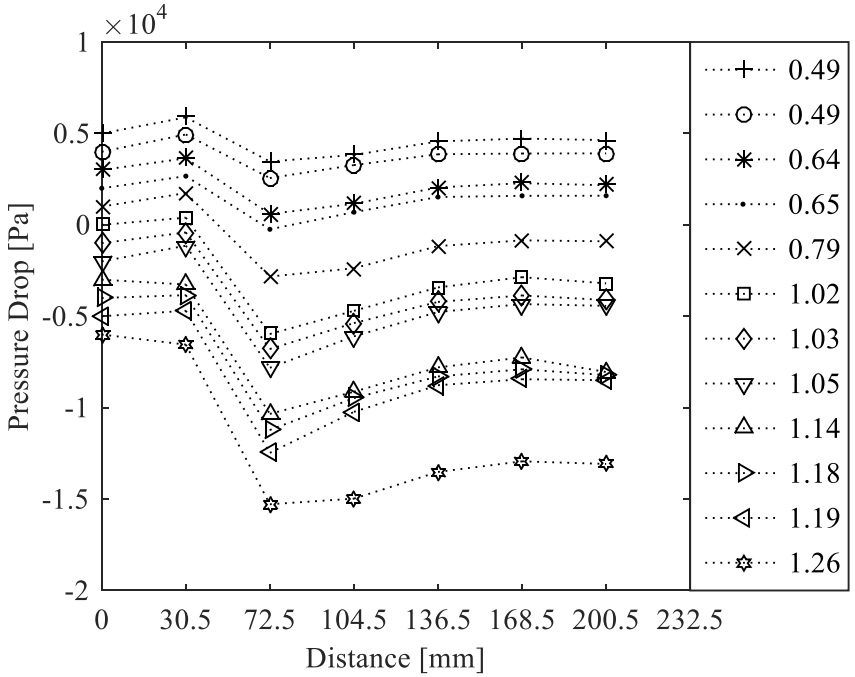


Source: Author (2020).

Figure 44 shows the effect of converging-diverging geometry on the pressure drop along the Venturi tube for stratified flows. Tendency lines were added to guide the eye. Results in Pa. Air mass flow rate ranged from 0.0002 to 0.0005 kg/s and water mass flow rate ranged from 0.27 to 0.39 kg/s. The mean void fraction ranged from 0.39 to 0.60.

For stratified patterns, the static pressure behavior is highly modified in relation to the ones shown in single-phase or bubbly flows. It is clear that flow disturbances induced by the 90º bend positioned 5 pipe diameters downstream the Venturi outlet caused unusual static pressure behavior. Recirculation zones were noticed by eye close to the 90º bend. Furthermore, the way the 90º bend affects the pressure behavior along the Venturi is modified when the water flow rate increases from 0.29 to 0.31 kg/s, or when the mean void fraction increases from 0.51 to 0.55.

For stratified flows with water flow rates equal to 0.27 and 0.29 kg/s, the lowest static pressure is located in the converging zone. Flow disturbances promoted by the 90º bend appeared to move the *vena contracta* towards the converging part. Note that the pressure

recovery in the diverging part was also affected, indicating that flow disturbances caused increasing dissipation effects.

For stratified flows with water flow rates equal to 0.31 and 0.39 kg/s, the lowest static pressure is located in the diverging zone. The manner the 90º bend affects the pressure behavior was modified. Flow disturbances promoted by the 90º bend appeared to move the *vena contracta* towards the diverging part. With these changes, dissipation and pressure loss along the Venturi were reduced.

Figure 44 - Effects of converging-diverging geometry and disturbances downstream the Venturi tube on the pressure drop for stratified flows. Tendency lines were added to guide the eye. Water flowrate in kg/s. Air flow rate ranged from 0.0002 to 0.0005 kg/s.

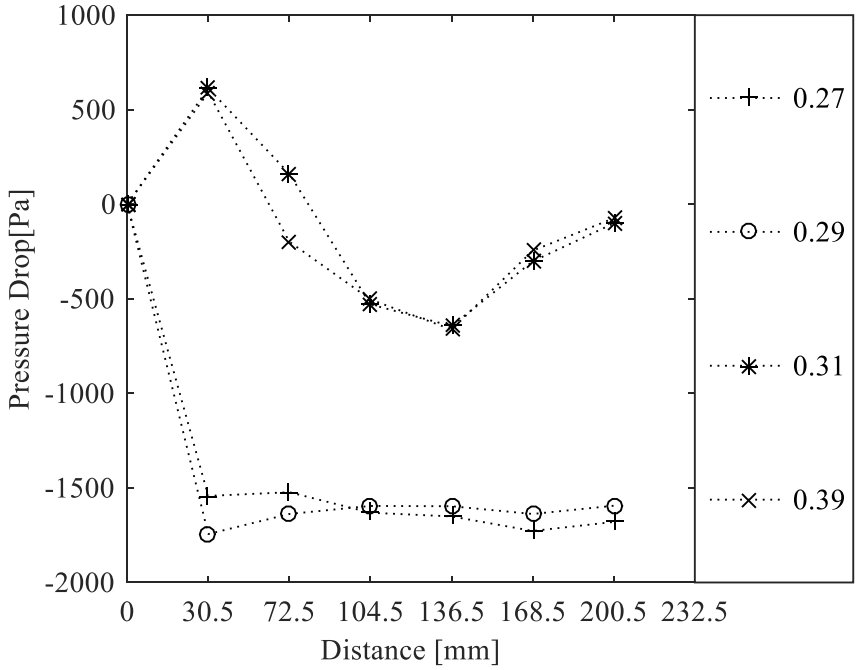


Source: Author (2020).

### 4.2.3 Flow pattern identification

In this section, the dynamic amplitude content of differential pressure signals along the Venturi and of mean concentration signals are analyzed for bubbly, slug and stratified flow patterns. Each experiment is investigated in a time span of 0.015 seconds. This value is sufficient to consider each flow experiment as a stationary process.

4.2.3.1 Pressure drop signals

Fast Fourier Transform (FFT) was applied to pressure drop signals along the Venturi tube. In order to apply the FFT, measurement frequencies must be high in order to describe the fastest two-phase flow scales. Measuring frequency adjusted to 60 Hz was sufficient for this purpose. Of course, only the dynamic amplitude content was analyzed: the instantaneous signal is subtracted from the ensemble average.

Figure 45 shows the effect of bubbly pattern on the Fast Fourier Transform of a differential pressure signal along the Venturi. The peak in the dynamic amplitude content occurs nearly in 15 Hz. The amplitude content is concentrated in a frequency band in the range 12-22 Hz.

Figure 45 – Effect of bubbly pattern on the Fast Fourier Transform of a differential pressure signal along the Venturi.

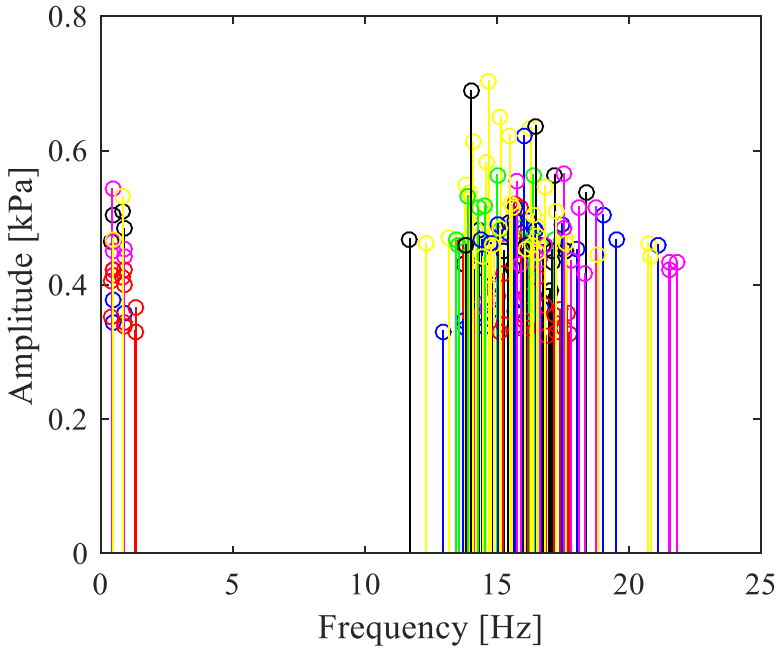


Source: Author (2020).

Table 4 shows the effects of the Venturi position and bubbly pattern on the mean standard deviation of the pressure difference. All pressure difference measurements are related to the Venturi inlet. Eleven experiments were performed with the air mass flow rate ranging from 0.0003 to 0.0018 kg/s and the water mass flow rate ranging from 1.9 to 2.26 kg/s. The mean void fraction ranged from 0.051 to 0.19. The highest mean standard

deviations were observed in a region which contains the Venturi throat and the converging inlet (taps 1 and 2).

Table 4 – Effects of the Venturi position and bubbly pattern on the mean standard deviation of the pressure difference. All pressure difference measurements are related to the Venturi inlet.

| Experiment | Converging part | Throat | Diverging part, tap 1 | Diverging part, tap 2 | Diverging part, tap 3 | Diverging part, tap 4 |
|---|---|---|---|---|---|---|
| 1 | 846,6 | 2060 | 2181 | 2047 | 1998 | 1689 |
| 2 | 762,9 | 1981 | 2095 | 2078 | 1948 | 1733 |
| 3 | 382 | 1883 | 2150 | 2011 | 2047 | 1893 |
| 4 | 346,1 | 1696 | 1918 | 1943 | 2116 | 1811 |
| 5 | 678,6 | 2055 | 3008 | 2727 | 2709 | 1989 |
| 6 | 426,9 | 2170 | 2713 | 2947 | 2147 | 1849 |
| 7 | 525,4 | 2402 | 2336 | 2750 | 2577 | 2080 |
| 8 | 386,8 | 2127 | 1996 | 2282 | 2543 | 2079 |
| 9 | 799,5 | 2283 | 2353 | 2610 | 2593 | 2181 |
| 10 | 481,3 | 2295 | 2675 | 2315 | 2315 | 1812 |
| 11 | 902,4 | 1930 | 2758 | 2274 | 2791 | 1929 |

Source: Author (2020).

Figure 46 shows the effect of slug pattern on the Fast Fourier Transform of a differential pressure signal along the Venturi. The peak in the dynamic amplitude content occurs nearly in 13 Hz. The dynamic amplitude content is concentrated in a frequency band in the range 7-14 Hz.

Table 5 shows the effects of the Venturi position and slug pattern on the mean standard deviation of the pressure difference. All measurements are related to the Venturi inlet. 19 experiments were performed with the air mass flow rate ranging from 0.0004 to 0.0036 kg/s and the water mass flow rate ranging from 0.49 to 1.26 kg/s. The mean void fraction ranged from 0.21 to 0.58. The highest mean standard deviations were observed in the Venturi throat. In the diverging region, the values of mean standard deviations were similar and higher than the ones found in the converging region.

Figure 46 - Effect of slug pattern on the Fast Fourier Transform of a differential pressure signal along the Venturi.

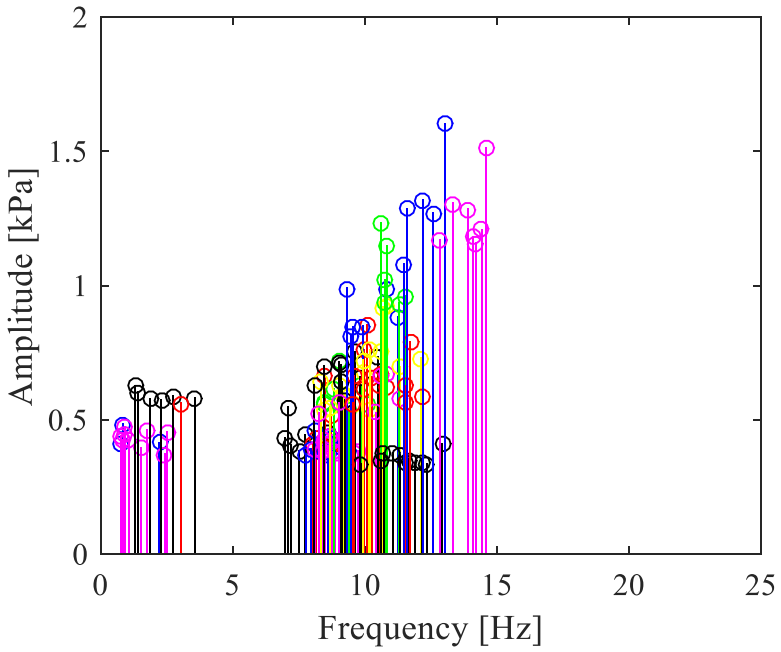


Source: Author (2020).

Table 5 – Effects of the Venturi position and slug pattern on the mean standard deviation of the pressure difference. All pressure difference measurements are related to the Venturi inlet.

| Experiment | Converging part | Throat | Diverging part, tap 1 | Diverging part, tap 2 | Diverging part, tap 3 | Diverging part, tap 4 |
|---|---|---|---|---|---|---|
| 1 | 722,9 | 1421 | 1255 | 1359 | 1445 | 1476 |
| 2 | 880,7 | 1533 | 1476 | 1367 | 1509 | 1616 |
| 3 | 914,9 | 1795 | 1475 | 1345 | 1437 | 1448 |
| 4 | 962,1 | 2063 | 1451 | 1304 | 1359 | 1360 |
| 5 | 1391 | 2259 | 1883 | 1888 | 1909 | 1964 |
| 6 | 1374 | 2468 | 1896 | 1788 | 1848 | 2081 |
| 7 | 1384 | 3084 | 1968 | 2035 | 2009 | 2146 |
| 8 | 1592 | 2805 | 1797 | 2236 | 2073 | 2213 |
| 9 | 2031 | 3978 | 2643 | 2378 | 2611 | 2716 |
| 10 | 1389 | 2537 | 1608 | 1831 | 1949 | 1983 |
| 11 | 1868 | 3322 | 2101 | 2365 | 2459 | 2582 |
| 12 | 2282 | 4276 | 3106 | 3292 | 3481 | 3354 |
| 13 | 1198 | 1833 | 1290 | 1392 | 1381 | 1331 |
| 14 | 1509 | 2618 | 1790 | 1975 | 2156 | 1754 |
| 15 | 2969 | 5069 | 3579 | 3763 | 3468 | 3910 |
| 16 | 2871 | 6680 | 4870 | 4370 | 4350 | 4669 |
| 17 | 565,2 | 585,7 | 553,8 | 606,4 | 603,1 | 584,6 |
| 18 | 564,2 | 580,7 | 552,2 | 574,3 | 581,1 | 591,3 |
| 19 | 576,2 | 603,4 | 559,7 | 608,9 | 536,6 | 555,3 |

Source: Author (2020).

Figure 47 shows the effect of stratified pattern on the Fast Fourier Transform of a differential pressure signal along the Venturi. The peak in the dynamic amplitude content occurs nearly in 8 Hz. The dynamic amplitude content is concentrated in a frequency band in the range 7-9 Hz. There is also meaningful amplitude content in a frequency band in the range 0-4 Hz.

Figure 47 - Effect of stratified pattern on the Fast Fourier Transform of a differential pressure signal along the Venturi.

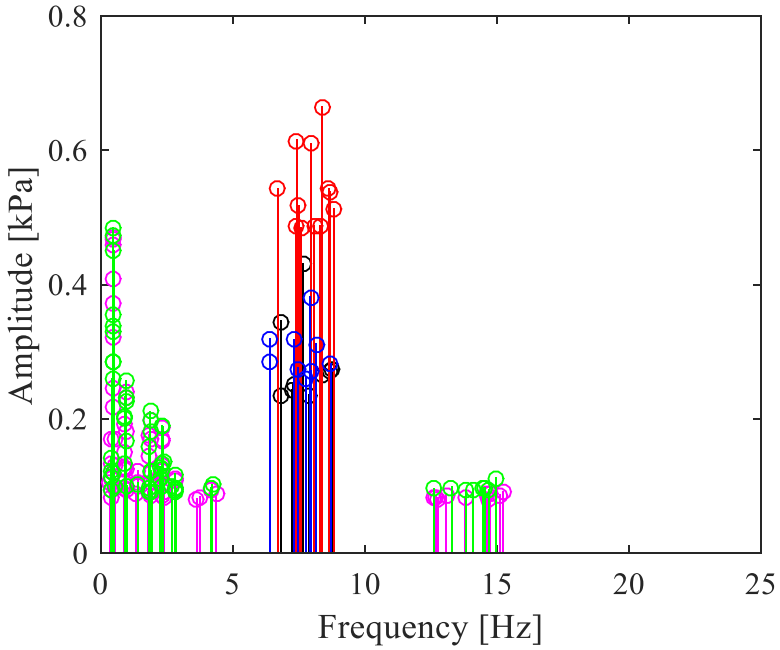


Source: Author (2020).

Table 6 shows the effects of the Venturi position and stratified pattern on the mean standard deviation of the pressure difference. All measurements are related to the Venturi inlet. 5 experiments were performed with the air mass flow rate ranging from 0.0002 to 0.0005 kg/s and the water mass flow rate ranging from 0.27 to 0.39 kg/s. The mean void fraction ranged from 0.39 to 0.60. The lowest mean standard deviations occurred in the Venturi converging part and the highest values, in the Venturi diverging region.

Table 6 – Effects of the Venturi position and stratified pattern on the mean standard deviation of the pressure difference. All pressure difference measurements are related to the Venturi inlet.

| Experiment | Converging part | Throat | Diverging part, tap 1 | Diverging part, tap 2 | Diverging part, tap 3 | Diverging part, tap 4 |
|---|---|---|---|---|---|---|
| 1 | 299,1 | 970,2 | 1244 | 1456 | 1471 | 1660 |
| 2 | 194 | 811,9 | 1025 | 860,5 | 945,4 | 982 |
| 3 | 457,2 | 695,8 | 740,4 | 852,5 | 835,9 | 944,6 |
| 4 | 608 | 599,9 | 601,4 | 603,1 | 573,7 | 633 |
| 5 | 631,9 | 631,6 | 641,2 | 632,7 | 599,8 | 632,6 |

Source: Author (2020).

Gas-liquid flow patterns could be determined in industrial applications by means of differential pressure signals obtained from a modified Venturi. The signals could serve as input for a dedicated algorithm to process the Venturi data. After FFT application on each signal, two information from the spectrum could be used for flow identification: the frequency where peak in the dynamic amplitude content occurs (8 Hz - stratified flow; 10 Hz - slug flow, 15 Hz - bubbly flow) and the frequency band where the dynamic amplitude content is concentrated (7-9 Hz, stratified flow; 7-14 Hz, slug flow; 12-22 Hz, bubbly flow). Of course, these values were obtained in the present working conditions and they would demand calibration in other applications.

Besides, simple flow statistics along the modified Venturi could provide extra information for flow pattern identification. The distribution of mean standard deviation values of differential pressure signals, for example, followed different trends for each flow pattern in the converging and diverging regions as well as in the Venturi throat.

#### 4.2.3.2 Mean concentration signals

Fast Fourier Transform (FFT) was applied to mean concentration signals in a given pipe cross-section. The same measuring frequency, 60 Hz, was applied. Mean concentration signals were obtained by Electrical Capacitance Tomography. Figure 48 shows the effect of bubbly pattern on the FFT of the mean concentration signal. The amplitude content is concentrated in a frequency band in the range 0 - 5 Hz.

Figure 48 - Effect of bubbly pattern on the Fast Fourier Transform of the mean concentration signal.

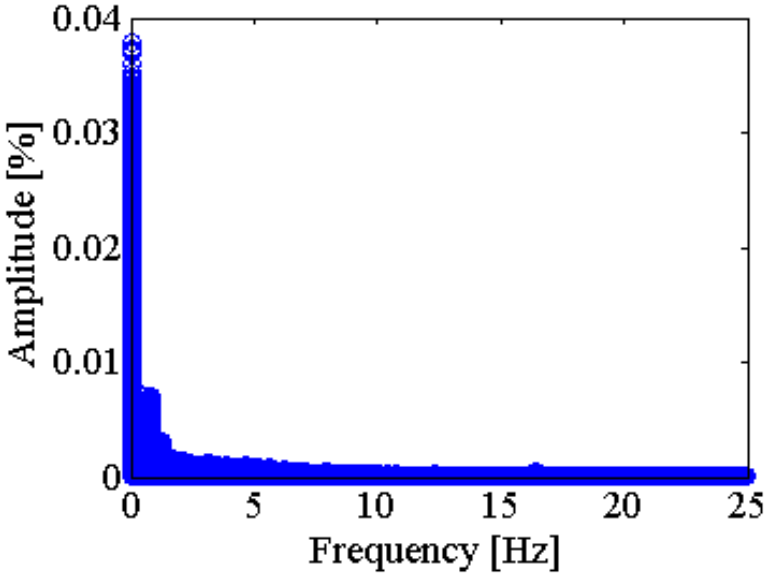


Source: Author (2020).

Table 7 shows the effect of the bubbly pattern on the void fraction mean standard deviation, $\sigma_\alpha$. $\sigma_\alpha$ varies between 0.010 and 0.012 in all experiments.

Table 7 – Effect of bubbly pattern on void fraction mean standard deviation, $\sigma_\alpha$.

| Experiment | $\alpha$ | $\sigma_\alpha$ |
|---|---|---|
| 1 | 0.95187 | 0.01027 |
| 2 | 0.95263 | 0.01073 |
| 3 | 0.94857 | 0.01155 |
| 4 | 0.94336 | 0.01230 |
| 5 | 0.95649 | 0.00996 |
| 6 | 0.94553 | 0.01151 |
| 7 | 0.94076 | 0.01215 |
| 8 | 0.95819 | 0.00973 |
| 9 | 0.95297 | 0.01032 |
| 10 | 0.94907 | 0.01167 |

Source: Author (2020).

Figure 49 shows the effect of slug pattern on the Fast Fourier Transform of the mean concentration signal in a given pipe cross-section. The dynamic amplitude content is significant in a frequency band in the range 0 - 15 Hz. Note that the peak in the dynamic amplitude content is one order of magnitude higher if compared to the one in bubbly pattern; compare Figures 48 and 49.

Figure 49 - Effect of slug pattern on the Fast Fourier Transform of the mean concentration signal.

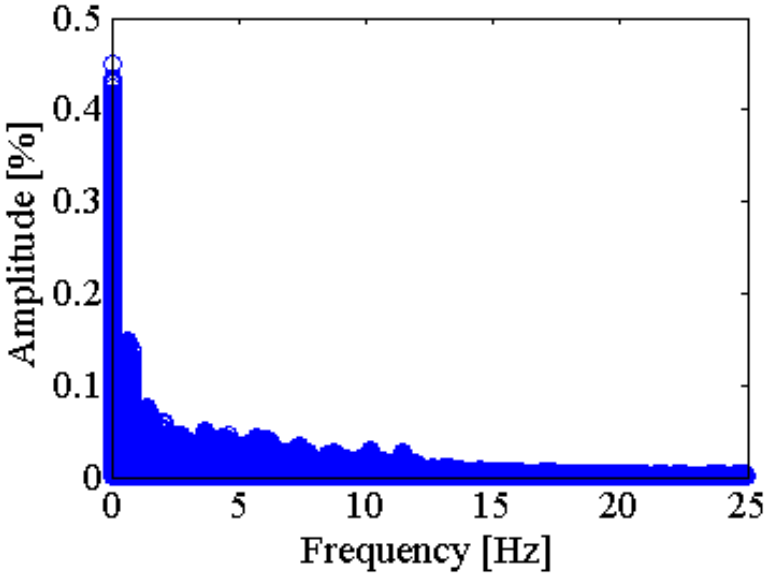


Source: Author (2020).

Table 8 shows the effect of the slug pattern on the void fraction mean standard deviation. $\sigma_\alpha$ ranges from 0.028 to 0.264 for all experiments.

Table 8 - Effect of slug pattern on void fraction mean standard deviation, $\sigma_\alpha$.

| Experiment | $\alpha$ | $\sigma_\alpha$ |
|---|---|---|
| 1 | 0.58893 | 0.25267 |
| 2 | 0.55193 | 0.26372 |
| 3 | 0.62551 | 0.22217 |
| 4 | 0.67699 | 0.17114 |
| 5 | 0.69826 | 0.12750 |
| 6 | 0.66053 | 0.18707 |
| 7 | 0.65089 | 0.19018 |
| 8 | 0.72047 | 0.10421 |
| 9 | 0.71672 | 0.11772 |
| 10 | 0.70866 | 0.14288 |
| 11 | 0.73433 | 0.07432 |
| 12 | 0.73168 | 0.10787 |
| 13 | 0.75976 | 0.05000 |
| 14 | 0.76396 | 0.06306 |
| 15 | 0.74216 | 0.07044 |
| 16 | 0.81568 | 0.02836 |
| 17 | 0.78977 | 0.04587 |
| 18 | 0.74525 | 0.06834 |
| 19 | 0.75285 | 0.07950 |

Source: Author (2020).

Figure 50 shows the effect of stratified pattern on the Fast Fourier Transform of the mean concentration signal. The dynamic amplitude content is significant in a frequency band in the range 0 - 5 Hz. Note that the peak in the dynamic amplitude content is twice the maximum value found for slug pattern; compare Figures 49 and 50. Note that the frequency where the dynamic amplitude peak is found, below 1 Hz, is nearly coincident for all flow patterns.

Figure 50 - Effect of stratified pattern on the Fast Fourier Transform of the mean concentration signal.

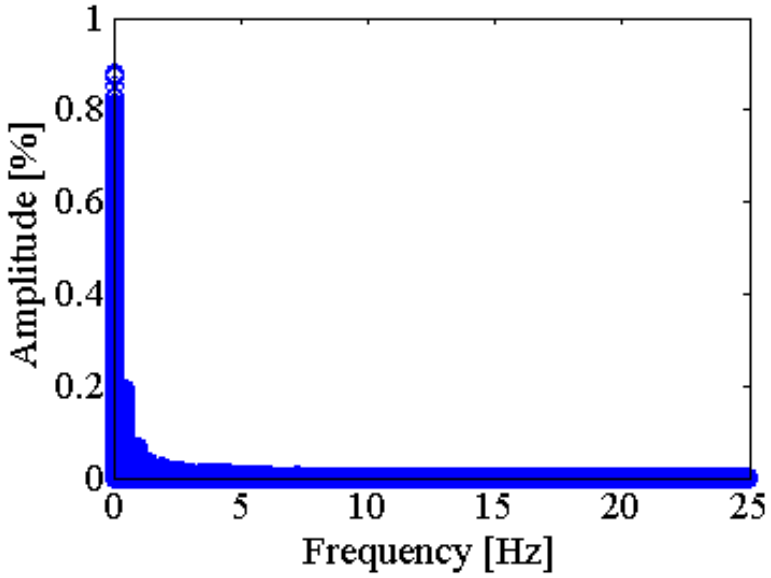


Source: Author (2020).

Table 9 shows the effect of the stratified pattern on the void fraction mean standard deviation. $\sigma_\alpha$ ranges from 0.31 to 0.38 for all experiments.

Table 9 - Effect of stratified pattern on void fraction mean standard deviation, $\sigma_\alpha$.

| Experiment | $\alpha$ | $\sigma_\alpha$ |
|---|---|---|
| 1 | 0.52174 | 0.37315 |
| 2 | 0.54211 | 0.36501 |
| 3 | 0.56900 | 0.33969 |
| 4 | 0.49236 | 0.38279 |
| 5 | 0.59369 | 0.30831 |

Source: Author (2020).

Figure 51 shows the effects of mean void fraction, $\alpha$, and flow pattern on the void fraction mean standard deviation, $\sigma_\alpha$. $\sigma_\alpha$ increases with increasing $\alpha$. $\sigma_\alpha$ can be as low as 0.01 for bubbly pattern and as high as 0.38 for stratified pattern.

Figure 51 – Effects of mean void fraction, α, and flow pattern on the void fraction mean standard deviation, $\sigma_\alpha$.

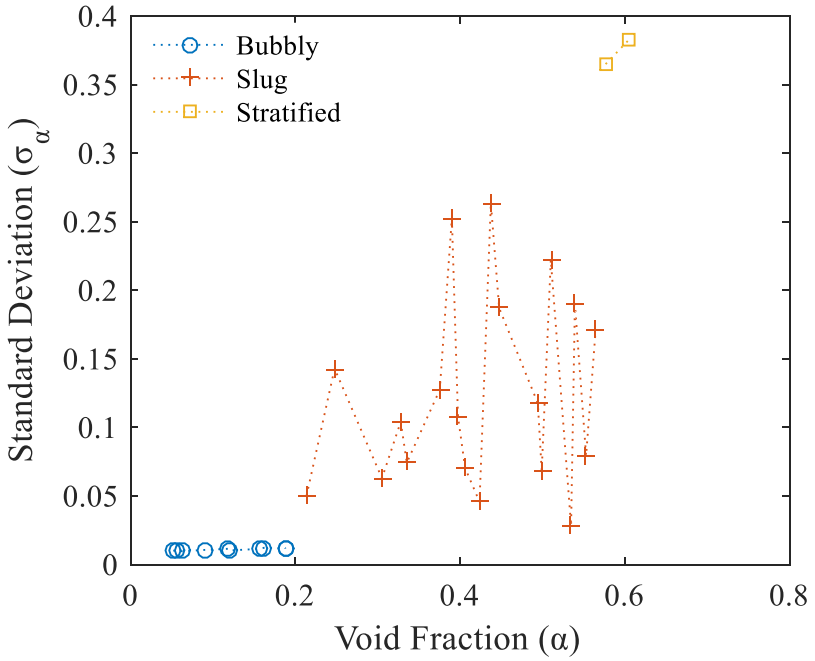


Source: Author (2020).

Gas-liquid flow patterns could be determined in industrial applications by means of concentration signals as well. The signals could serve as input for a dedicated algorithm to process the data. After FFT application on each signal, two information from the spectrum could be used for flow identification: the peak value in the dynamic amplitude content (0.5-0.9 % - stratified flow; 0.05-0.45 % - slug flow, 0.02-0.04 % - bubbly flow) and the frequency band where the dynamic amplitude content is mostly concentrated (0-5 Hz, stratified flow; 0-15 Hz, slug flow; 0-5 Hz, bubbly flow). Besides, simple flow statistics could provide extra information for flow pattern identification such as the mean concentration or void fraction, and the void fraction mean standard deviation, $\sigma_\alpha$. The following values of $\sigma_\alpha$ were obtained for each pattern: 0.300 to 0.390, stratified flow; 0.020 to 0.270, slug flows; 0.009 to 0.015, bubbly flows. Obviously, these values were obtained in the present working conditions and they would demand calibration in other applications.

Table 10 summarizes characteristics of each flow pattern in order to allow flow pattern identification.

Table 10 - Summary of flow pattern characteristics.

| **Pattern identification criteria** | **Bubbly flows** | **Slug flows** | **Stratified flows** |
|---|---|---|---|
| Frequency of peaking amplitude - ΔP [Hz] | 15 | 10 | 8 |
| Frequency band with high amplitude content - ΔP [Hz] | 12 – 22 | 7 -14 | 7 – 9 |
| Position of maximum $\sigma_{\Delta P}$ | Diverging region inlet | Venturi throat | Diverging region outlet |
| Frequency band with high Amplitude content – α [Hz] | 0-5 | 0-15 | 0-5 |
| Value of peaking Amplitude - [%] | 0.020 – 0.040 | 0.050 – 0.450 | 0.500 – 0.900 |
| α | 0.94076 – 0.95819 | 0.55193 – 0.81568 | 0.49236 – 0.59369 |
| $\sigma_\alpha$ | 0.009 – 0.015 | 0.020 – 0.270 | 0.300 – 0.390 |

Source: Author (2020).

# 5 CONCLUSIONS

Two phase air-water flows were measured by means of a modified Venturi tube, transmission-reception ultrasound sensors and Electrical Capacitance Tomography in a multiphase flow rig. Tests were also performed in static columns to determine concentrations of water-crude oil-air mixtures via pulse-echo technique. A TDC1000-TDC7200 EVM board from Texas Instruments was configured to control ultrasonic emission and reception from piezoelectric elements, measuring the elapsed Time of Flight between pulses.

The dynamic analysis of concentration and differential pressure signals were performed via Fast Fourier Transform. The static pressure behavior along a Venturi were measured for bubbly, slug and stratified patterns. Single-phase and two-phase mass flow rate measurements have been analyzed with a modified Venturi tube and transmission-reception ultrasound sensors.

The main remarks, results and conclusions of this work are presented below:

- An inexpensive method based on pulse-echo technique was developed to determine sound speed values for crude oil samples;
- The effect of the column height on pulse-echo concentration measurements in water-crude oil-air static columns was determined. The minimum measuring heights for water and crude oil were equal to 15 and 10 mm, respectively. The same measuring system can be applied to determine concentrations in water-air, crude oil-air and water-crude oil-air static columns;
- The effect of void fraction on liquid mass flowrate measurements for a commercial ultrasound meter was determined in horizontal and vertical gas-liquid flows. Ultrasound measurements underestimated the liquid mass flow rate in horizontal flow direction and mostly overestimated in vertical direction. It was identified limiting working conditions: measurements were only possible for void fractions less than 0.18 in horizontal flows, and less than 0.32 in vertical flows.
- In the presence of air, liquid mass flow rates are overestimated by a Venturi meter, particularly for mean void fractions over 0.2. A correction function based on the mean void fraction can provide appropriate estimations;

- The effect of converging-diverging geometry on the pressure drop along the Venturi tube was measured for water single-phase flows. The decrease in static pressure is subtle in the converging geometry and occurs sharply in the Venturi throat where the *vena contracta* is located. A fully developed single-phase flow was measured;
- The effect of converging-diverging geometry on the pressure drop along the Venturi tube was measured for bubbly, slug and stratified flow patterns. For bubbly patterns, the static pressure behavior is similar to the one observed in single-phase flows. For slug patterns, the static pressure behavior is slightly modified in comparison to bubbly flows. For stratified patterns, changes in the static pressure behavior are significant. Flow singularities (a 90º bend positioned 5 pipe diameters downstream the Venturi outlet) caused unusual static pressure behavior. With increasing liquid flow rate, the *vena contracta* can be displaced from the converging to the diverging region.
- Concentration measurements can be used to determine flow patterns. Besides typical flow statistics such as mean void fraction and standard deviation of the void fraction, the dynamic amplitude content can assist on flow pattern identification;
- Differential pressure signals along a modified Venturi can also be used to determine flow patterns. Besides typical flow statistical moments, the dynamic amplitude content can assist on flow pattern identification. Spectrum information obtained by Fast Fourier Transform can provide identification pattern criteria; i.e. the frequency where a peak in the dynamic amplitude content occurs and the frequency band where the dynamic amplitude content is concentrated. Furthermore, the distribution of mean standard deviation values of differential pressure signals followed different trends for each flow pattern in the converging and diverging regions as well as in the Venturi throat.

So is possible to identify flow patterns using a modify Venturi tube or a sensor that measures the concentration (in this case a CT scanner). To measure multiphase flows using ultrasonic and Venturi tube meters with the results presented is better to use the ultrasonic meter to measure each phase concentration and the Venturi tube to measure liquid flow velocity.

# REFERENCES

BECK, M.; WILLIAMS, R. A. Process tomography: a European innovation and its applications. Measurement Science and Technology, IOP Publishing, v. 7, n. 3, p. 215,1996.

BRASSIER, P.; HOSTEN, B.; VULOVIC, F. High-frequency transducers and correlation method to enhance ultrasonic gas flow metering. Flow measurement and instrumentation, Elsevier, v. 12, n.3, p. 201-211, 2001.

BRITTO, I. Caracterização de Falhas em Materiais Compósitos Utilizando Tomografia. XXXII Congresso Nacional de Ensaios não Destrutivos e Inspeção. 14p.2014.

BUENOS, Alexandre Aparecido. Avaliação de tensão residual gerada pelo processo de usinagem utilizando acoustoelasticidade. 2010. 205p. Dissertação (Mestrado) - Faculdade de Engenharia Mecânica, Universidade Estadual de Campinas, Campinas.

CARVALHO, R. D. M.; VENTURINI, O. J.; TANAHASHI, E. I.; NEVES JR., F.; FRANÇA, F. A. Application of the ultrasonic technique and high-speed filming for the study of the structure of air–water bubbly flows. Experimental Thermal and Fluid Science, v. 33, n. 7, p. 1065-1086, 2009.

CAVALCANTI, V. Y. S. d. L. et al. Simulação computacional de um tomógrafo capacitivo elétrico paralelo aplicado ao processo adsortivo. Universidade Federal da Paraíba, 2009.

ÇENGEL, Yunus A.; CIMBALA, John M. Mecânica dos Fluidos: Fundamentos e Aplicações. São Paulo: McGrawHill, Bookman, AMGH, 2007. XXVI.

CHEEKE, N. D. J.. Fundamentals and applications of ultrasonic waves. Boca Raton: CRC Press LLC, 2002. 462 p.

CHRISTOPHER, E. B. Fundamentals of multiphase flows. Cambridge University, Press UK, 2005.

CORNELIUSSEN, S. et al. Handbook of multiphase flow metering. Norwegian Society for Oil and Gas Measurement (NFOGM), Revision, v. 2, 2005.

COLLIER, J. G. e THOME, J. R. Convective Boiling and Condensation. New York: Oxford University Press Inc. 1996.

DACIUK, R. J. Estudo de parâmetros ultra-sônicos para caracterização de líquidos. Dissertação de Mestrado. 2008. 90f. Universidade Tecnológica Federal do Paraná, 2008.

FACCINI, J. L. H. Estudo de Escoamentos Bifásicos Usando Técnicas Ultra-Sônicas. Tese de Doutorado. 2008. 177f. Universidade Federal do Rio de Janeiro, 2008.

FOSS, B.; KNUDSEN, B. R.; GRIMSTAD, B. Petroleum production optimization a static or dynamic problem? Computers & Chemical Engineering, Elsevier, v. 114, p.245–253, 2018.

GREEN, P. J. Bayesian reconstructions from emission tomography data using a modified EM algorithm. IEEE transactions on medical imaging, Citeseer, v. 9, n. 1, p. 84–93, 1990.

HALLIDAY, R.;RESNICK,R.; WALKER, J.. Fundamentos de Física, Volume 2: Gravitação, Ondas e Termodinâmica. Rio de Janeiro: LTC, 2012.

HAYES, D.; GREGORY, I.; BECK, M. Velocity profile measurement in oil/gas flows. IET, 1995.

KINSLER, L. E. et al. Fundamentals of acoustics. Fundamentals of Acoustics, 4th Edition, by Lawrence E. Kinsler, Austin R. Frey, Alan B. Coppens, James V. Sanders, pp. 560.ISBN 0-471-84789-5. Wiley-VCH, December 1999, p. 560, 1999.

LE, A. Ultrasonic sensing basics for liquid level sensing, flow sensing, and fluid identification applications, snaa220a.TEXAS Instruments, 2015.

LIANG, F. et al. Gas-liquid two-phase flow pattern identification by ultrasonic echoes reflected from the inner wall of a pipe. Measurement Science and technology, IOP Publishing, v. 27, n. 3, p. 035304, 2016.

LIPTAK, B. G. Instrument Engineers' Handbook, Volume One: Process Measurement and Analysis. [S.I.]: CRC press, 2003.

LORENTZEN, R. J. et al. Soft multiphase flow metering for accurate production allocation (russian). In: SOCIETY OF PETROLEUM ENGINEERS. SPE Russian Oil and Gas Conference and Exhibition [S.l.], 2010.

MURAI, Y. et al. Development of an ultrasonic void fraction profiler. Measurement Science and Technology, IOP Publishing, v. 20, n. 11, p. 114003, 2009.

MURAKAWA, H.; KIKURA, H.; ARITOMI, A. Application of ultrasonic Doppler method for bubbly flow measurement using two ultrasonic frequencies. Experimental Thermal and Fluid Science, Elsevier, v. 29, p. 843–850, 2005.

MURAKAWA, H.; KIKURA, H.; ARITOMI, M. Application of ultrasonic multi-wave method for two-phase bubbly and slug flows. Flow measurement and instrumentation, Elsevier, v. 19, n. 3-4, p. 205–213, 2008.

OFUCHI, C. Y.. Técnicas avançadas para análise de escoamentos bifásicos gás-liquido em golfadas. Dissertação - Universidade Tecnológica Federal do Paraná, 2011.

OLIVEIRA, J. L. G. et al. Mass flow rate measurements in gas–liquid flows by means of a Venturi or orifice plate coupled to a void fraction sensor. Experimental Thermal and Fluid Science, Elsevier, v. 33, n. 2, p. 253–260, 2009.

PANAMETRICS. Two-Channel TransPort Mod. 2PT868 Portable Flowmeter. User's Manual. PANAMETRICS, Inc., Waltham, MA, USA, 1997.

PROCESS TOMOGRAPHY. Electrical capacitance tomography system: Fundamentals of ECT. Wilmslow: Process Tomography Ltd, United Kingdom, 2009.

QIN, R.; DUAN, C. The principle and applications of Bernoulli equation. In: IOP PUBLISHING. Journal of Physics: Conference Series. [S.l.], 2017. v. 916, n. 1, p. 012038.

ROSE, J. L.. Ultrasonic waves in solid media. New York: Cambridge University Press, 1999. 454p.

S, CHEAUA, F. D. Theoretical approaches regarding the Venturi effect Hydraulic, n. 3, 2016.

SANTOS, M. G. de P.; BÉTTEGA, R. Avaliação dos parâmetros de projeto de medidores de vazão tipo venturi utilizando fluidodinâmica computacional.Blucher Chemical Engineering Proceedings, v. 1, n. 3, p. 2159–2164, 2015.

SOARES, M. B.. Estudo de um tomógrafo capacitivo elétrico paralelo aplicado ao processo adsortivo. Universidade Federal da Paraíba, 2009.

SOUSA, J. M. d. Análise da integridade estrutural em dutos de condução de petróleo e gás com incidência de mossas. Universidade Federal de Pernambuco, 2017.

SU, Q.; TAN, C.; DONG, F. Mechanism modeling for phase fraction measurement with ultrasound attenuation in oil–water two-phase flow. Measurement Science and Technology, IOP Publishing, v. 28, n. 3, p. 035304, 2017.

THORN, R.; JOHANSEN, G. A.; HJERTAKER, B. Three-phase flow measurement in the petroleum industry. Measurement Science and Technology, IOP Publishing, v. 24, n. 1, p. 012003, 2012.

TOMOFLOW LTD (United Kingdom). User Manual Tomoflow**:** Flowan v1.33. Dorchester: Tomoflow Ltd, 2003.

VATANAKUL, M.; ZHENG, YING; COUTURIER, M. Application of Ultrasonic Technique in Multiphase Flows. Ultrasonics, p. 5681-5691, 2004.

WADA, S.; KIKURA, H.; ARITOMI, M. Pattern recognition and signal processing of ultrasonic echo signal on two-phase flow. Flow Measurement and Instrumentation, Elsevier, v. 17, n. 4, p. 207–224, 2006.

WARREN, T.; WILCOX, D. R. Feasibility study of capacitive tomography. In: Proceedings of the 2006 International Conference on Image Processing, Computer Vision and Pattern Recognition, Las Vegas, NV: June 26-29, 2006.

# ANNEX A – Uncertainty Analysis

Turbulent flows are often analyzed as a stochastic process. Difficulties are higher in two-phase flow analysis. Statistics are necessary to quantify flow variables (i.e. static pressure, void fraction, velocity field etc.) and their variations. Flow measurement results consist of a mean value and an interval which delimits the measurement uncertainty. The uncertainty determination of indirectly calculated parameters is performed through an error propagation process. The uncertainty of a result $y$, $U_c(y)$, is given through:

$$U_c(y) = \sqrt{\sum_{i=1}^{n} \left[\frac{\partial f}{\partial x_i}\right]^2 U^2(x_i)} \tag{A1}$$

where $x_i$ stand for independent variables and $f$ is the function that relates the calculated parameter to the independent quantities.

## A.1 Sound Speed

Concentration and column height uncertainties, $U_{\varsigma'}$ and $U_{h_c}$, respectively, are given as follows:

$$U_{\varsigma'} = \sqrt{\left(\frac{2}{(Vs_{H_2O}ToF)-(Vs_{oil}ToF)}\right)^2 U_h^2 + \left(\frac{2h}{(Vs_{\varsigma}-Vs_{oil})ToF^2}\right)^2 U_{ToF}^2} \tag{A2}$$

$$U_{h_c} = \sqrt{\left(\frac{(\varsigma' Vs_{H_2O} + |1-\varsigma'|Vs_{oil})}{2}\right)^2 U_{\varsigma'}^2 + \left(ToF\left(\frac{(\varsigma'-1)Vs_{oil}}{2|1-\varsigma'|} + \frac{Vs_{H_2O}}{2}\right)\right)^2 U_{ToF}^2} \tag{A3}$$

where $ToF$ is the Time of Flight in seconds, $h$ the column height of liquid in meters, $\varsigma'$ the calculated water fraction (%), $Vs_{H_2O}$ the sound speed in water and $Vs_{oil}$ the sound speed in crude oil.

### A.2 Mass Flow Rate - Venturi

The uncertainty of the mass flow rate obtained with the Venturi meter, $U_{m_v}$, is given by:

$$U_{m_v} = \sqrt{\left(\frac{C_d A Y F_a}{\sqrt{1-\beta^4}}\sqrt{2\rho}\,\frac{1}{2\sqrt{\Delta p}}\right)^2 U_{\Delta p}^2 + \left(\frac{C_d Y F_a}{\sqrt{1-\beta^4}}\sqrt{2\rho\Delta p}\right)^2 U_A^2} \quad \text{(A4)}$$

where $A$ represents the Venturi throat area, $\beta$ the throat to pipe diameter ratio, $\rho$ the mass density, $C_d$ the discharge coefficient, $Y$ the compressibility coefficient, $\Delta p$ the pressure difference and $F_a$ the thermal expansion correction factor.

### A.3 - Mass Flow Rate - Ultrasound

The uncertainty of the mass flow rate obtained with the Ultrasonic meter, $U_{m_{U.S.}}$, is given by:

$$U_{m_{U.S.}} = \sqrt{(\rho_l A`)^2 U_v^2 + (\rho_l v)^2 U_{A`}^2} \quad \text{(A5)}$$

where $\rho_l$ and $A$` represent the liquid mass density and the cross-section area, respectively.

### A.4 Air mass Density

The uncertainty of the air mass density, $U_{\rho_g}$, is given by:

$$U_{\rho_g} = \sqrt{\left(\frac{1}{287.0856(273+temp)}\right)^2 U_p^2 + \left(-\frac{0.00348328p-352.944}{(273+temp)^2}\right)^2 U_{temp}^2} \quad \text{(A6)}$$

where $p$ is the static pressure and $temp$, the temperature.

### A.5 Air Mass Flow Rate

The uncertainty of the air mass flow rate obtained with the anemometer, $U_{m_{air}}$, is given by:

$$U_{m_{air}} = \sqrt{\left(\rho_g A`\right)^2 U_v^2 + (vA`)^2 U_{\rho_g}^2 + \left(\rho_g v\right)^2 U_{A`}^2} \tag{A7}$$

where $\rho_g$ is the air mass density and $v$ the air bulk velocity measured by the anemometer.

### A.6 Quality

The quality uncertainty, $U_x$, is given by:

$$U_x = \sqrt{\left(\frac{m_{coriolis}}{(m_{air}+m_{coriolis})^2}\right)^2 U_{m_{air}}^2 + \left(-\frac{m_{air}}{(m_{air}+m_{coriolis})^2}\right)^2 U_{m_{coriolis}}^2} \tag{A8}$$

where $m_{coriolis}$ is the liquid mass flow rate measured by the Coriolis meter and $m_{air}$ the air mass flow rate.

### A.7 Void Fraction

The void fraction uncertainty, $U_\alpha$, is given by:

$$U_\alpha = \sqrt{\left(\frac{\left(\rho_g S\frac{1-x}{x}\right)}{\left(\left(\rho_g S\frac{1-x}{x}\right)+\rho_l\right)^2}\right)^2 U_{\rho_g}^2 + \left(\frac{\left(\frac{\rho_g}{\rho_l}S\right)}{\left(\left(\frac{\rho_g}{\rho_l}S(-x)\right)+\left(\frac{\rho_g}{\rho_l}S\right)+x\right)^2}\right)^2 U_x^2} \tag{A9}$$

where $S$ is the mean slip ratio and $x$, the quality.

## APPENDIX A – Source Code for Data Acquisition via Wireless Communication

Pressure drop data along the Venturi meter were transferred wireless. An onboard microcontroller is responsible for data acquisition from the bench, while a second one with the same characteristics and connected to a personal computer receives the transmitted data. Data storage and reading are performed via a software developed in LabVIEW platform. The source code is presented below. Figure 52 presents the source code flowchart for pressure drop data acquisition.

Figure 52 – Source code flowchart for pressure drop data acquisition.

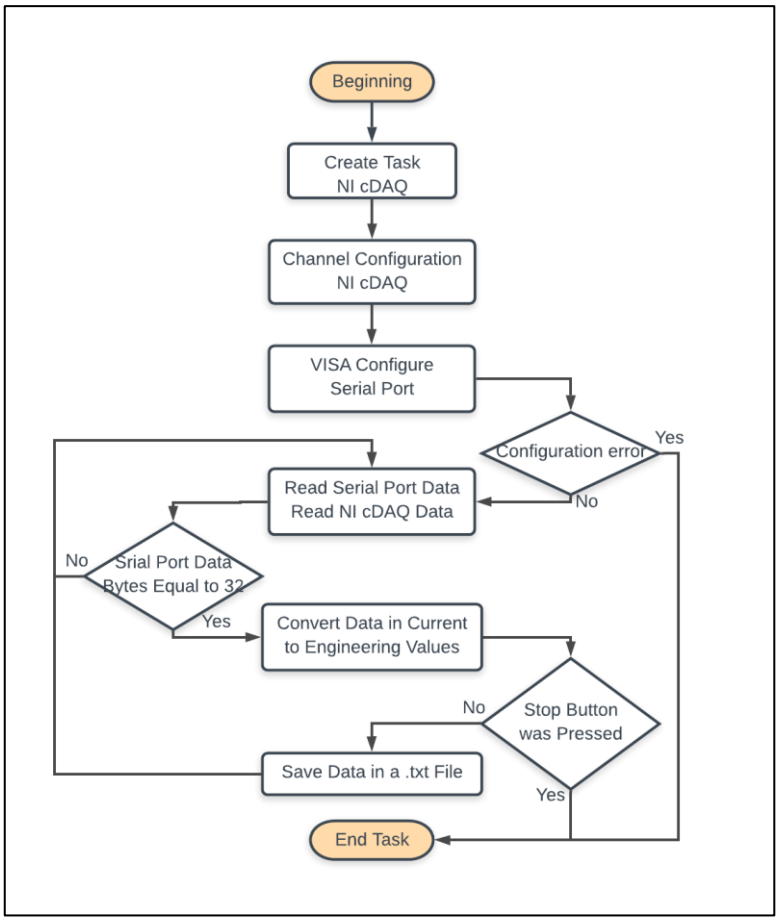


Source: Author (2019).

Figures 53-59 demonstrate the source code for data acquisition as block diagrams. Figures 53 and 54 illustrate block diagrams of the channel configuration blocks to cDAQ and of the VISA serial configuration, respectively. Figure 55 presents the block diagram for data reading from USB serial port. Figure 56 presents the diagram for converting input current signal into

differential pressure. The conversion occurs for eight differential pressure channels. Figure 57 presents the diagram for converting input current signal into absolute pressure and mass flow rate. Figure 58 presents the diagram for data storage in .txt files. Figure 59 presents the diagram for USB and cDAQ communication completion.

Figure 53 – Block diagram of channel configuration blocks to cDAQ.

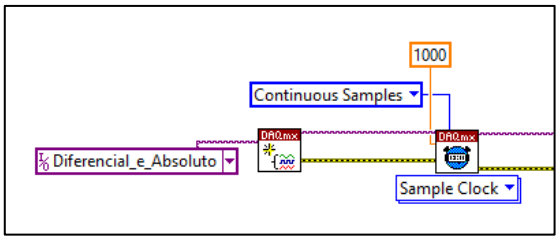


Source: Author (2019).

Figure 54 – Block diagram of VISA serial configuration.

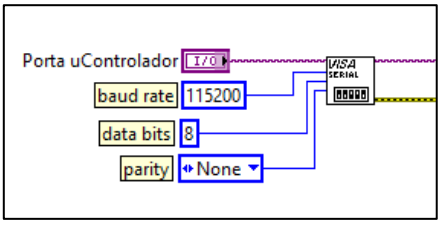


Source: Author (2019).

Figure 55 – Block diagram for data reading from USB serial port.

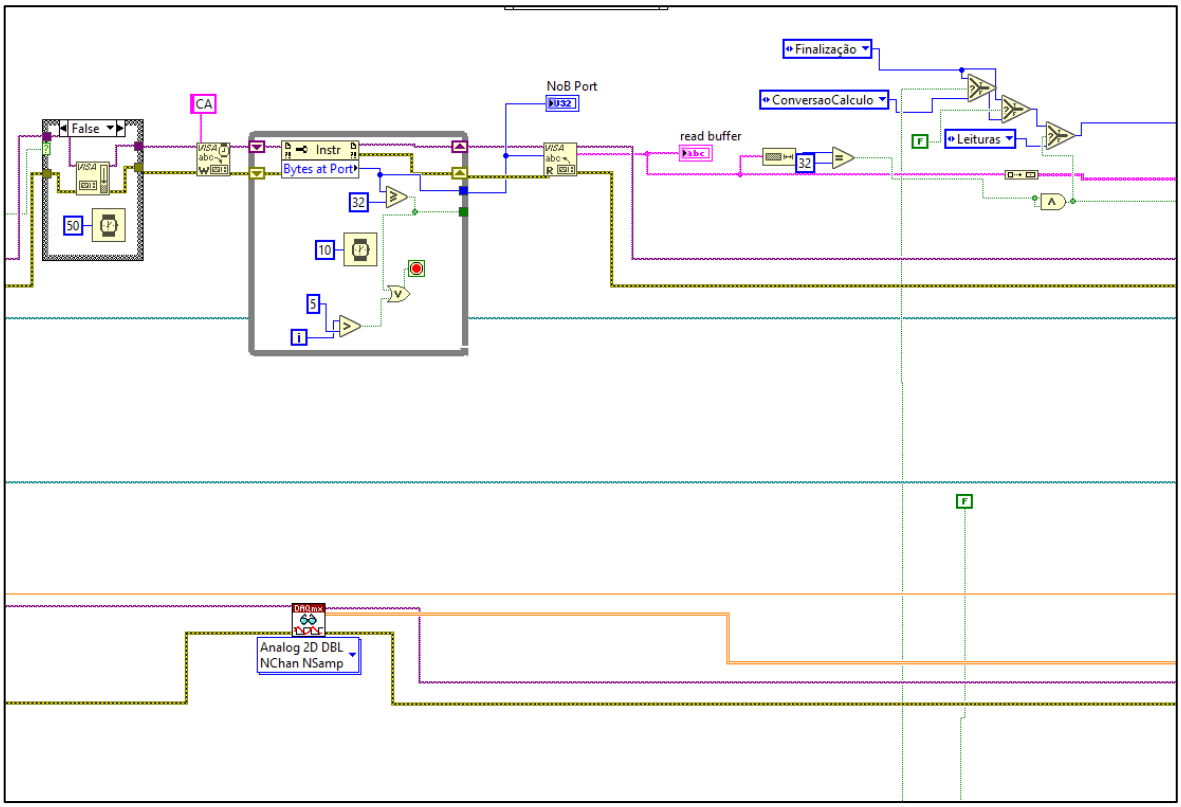


Source: Author (2019).

Figure 56 – Block diagram for converting input current signal into differential pressure.

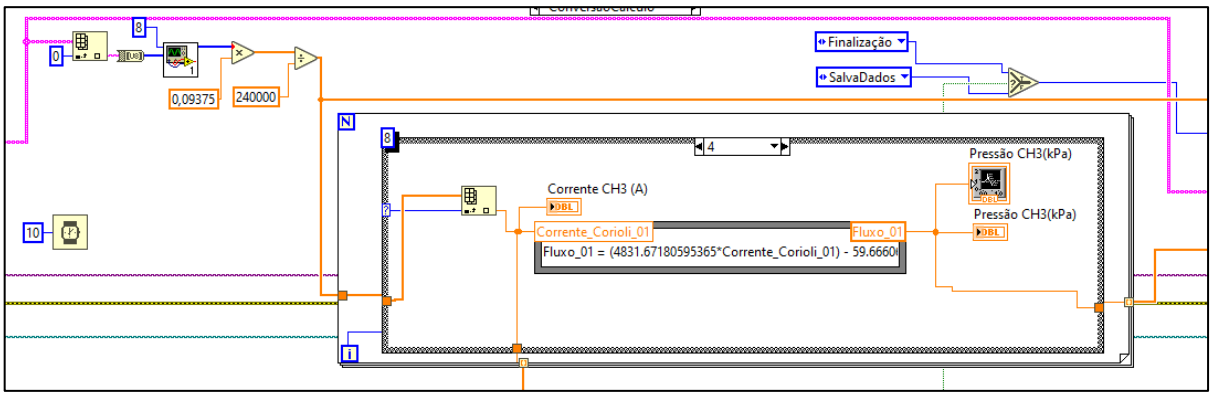


Source: Author (2019).

Figure 57 - Block diagram for converting input current signal into absolute pressure and mass flow rate.

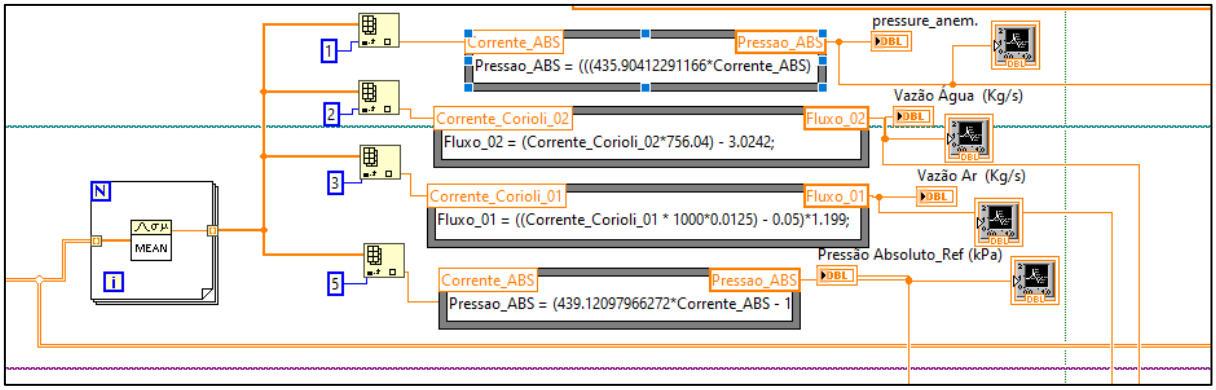


Source: Author (2019).

Figure 58 – Block diagram for data storage in .txt files.

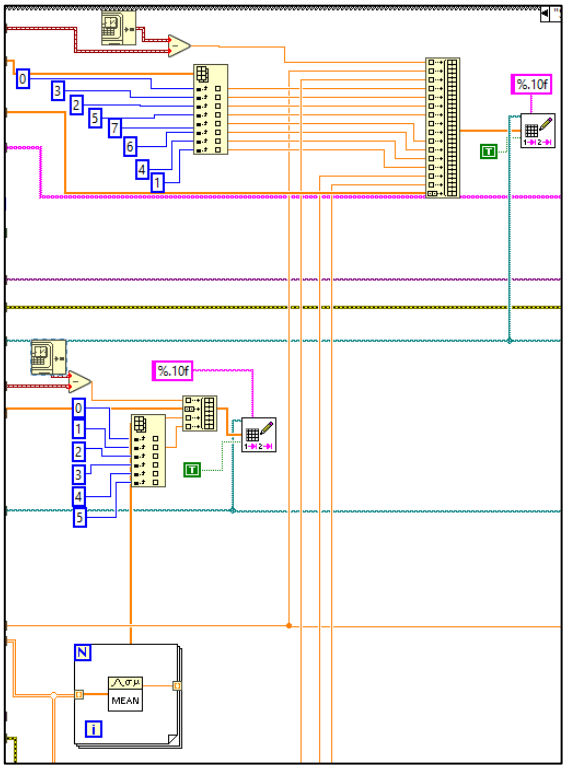


Source: Author (2019).

Figure 59 – Block diagram for USB and cDAQ communication completion.

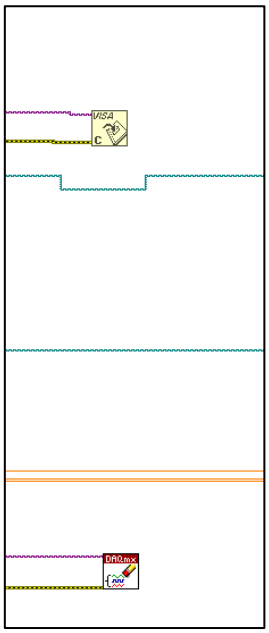


Source: Author (2019).

## APPENDIX B – Source Code for Data Acquisition via Serial Communication

Mass flow rate, temperature and absolute pressure data were transferred via serial communication. Data transmission occurred through an acquisition module of National Instruments CDaQ-9178. Data storage and reading are performed via software in LabVIEW platform. The source code is presented below. Figure 60 presents the source code flowchart for data acquisition via serial communication.

Figure 60 – Source code flowchart for data acquisition via serial communication.

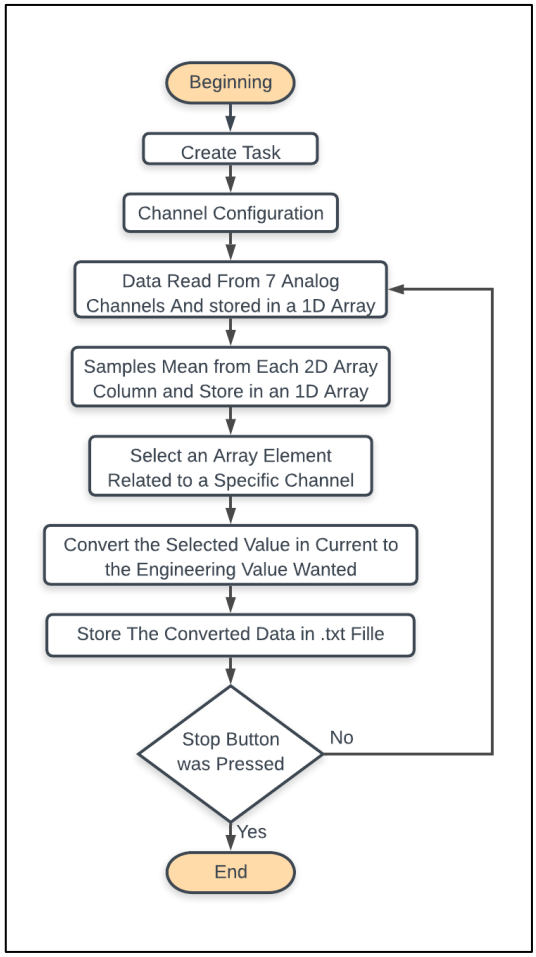


Source: Author (2019).

Figures 61-64 demonstrate the source code for data acquisition as block diagrams. Figure 61 presents the block diagram of channel configurations. Figure 62 presents the block diagram for calculating the mean mass flow rate, temperature and absolute pressure in a given period. Figure 63 presents the diagram for converting input current signal into mass flow rate. Figure 64 presents the diagram for data storage in .txt files.

Figure 61 - Block diagram of channel configurations.

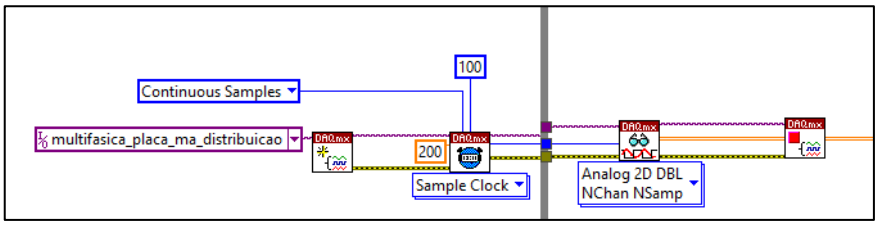


Source: Author (2019).

Figure 62 - Block diagram for calculating the mean mass flow rate, temperature and absolute pressure.

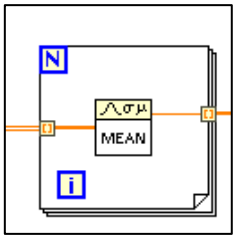


Source: Author (2019)

Figure 63 – Block diagram for converting input current signal into mass flow rate and absolute pressure.

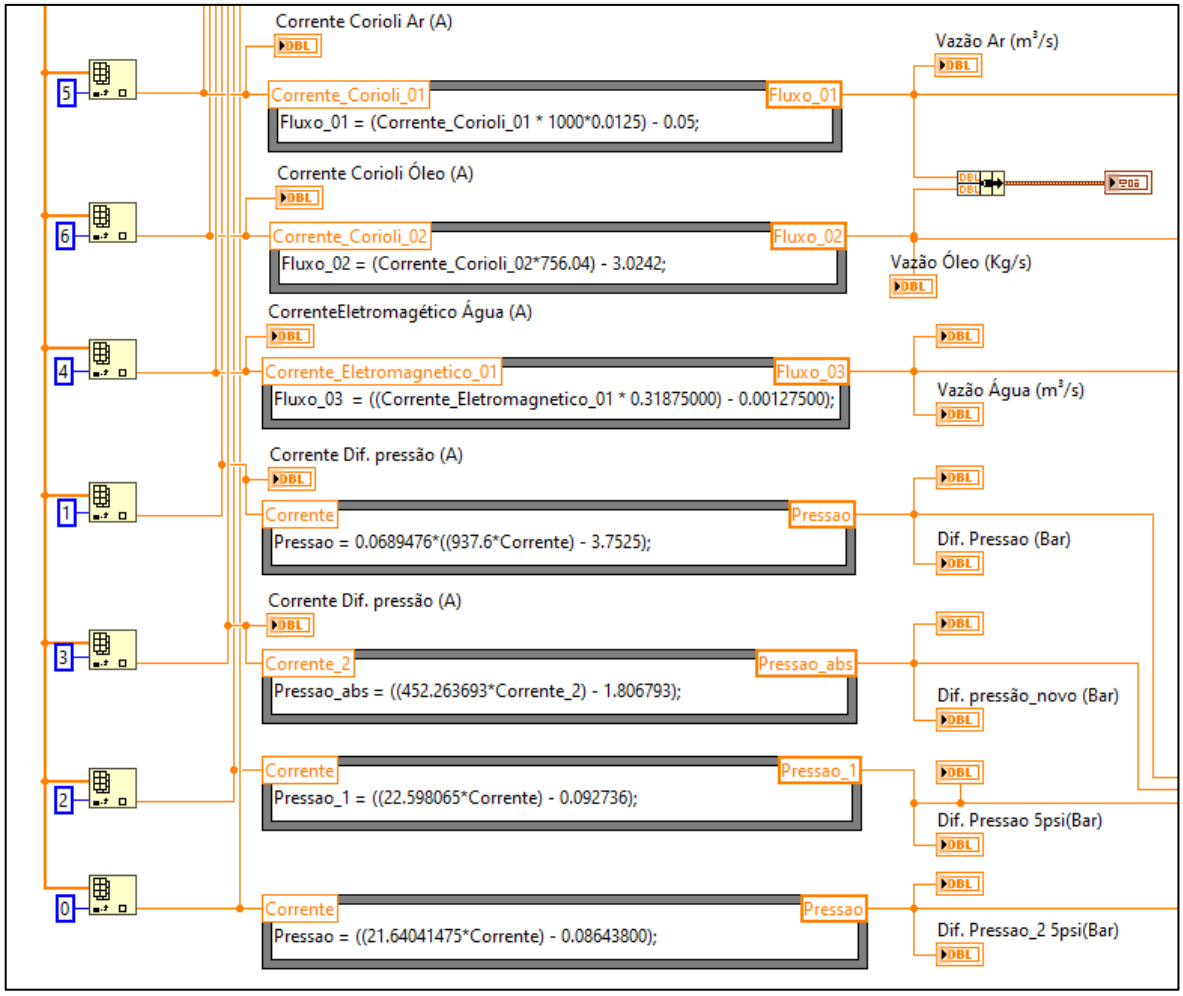


Source: Author (2019).

Figure 64 - Block diagram for data storage in .txt files.

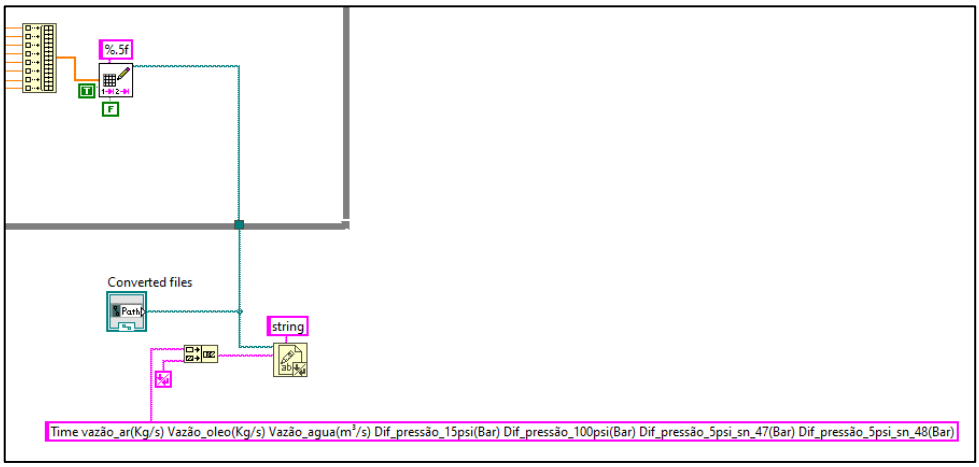


Source: Author (2019).